Thermal and decompression history of the Lanzo Massif, northern Italy: Implications for the thermal structure near the lithosphere–asthenosphere boundary

Tomo Aoki, Kazuhito Ozawa, Jean-Louis Bodinier, Françoise Boudier, Yuto Sato

Lithos 372–373 (2020) 105661

Contents lists available at ScienceDirect

Lithos

journal homepage: www.elsevier.com/locate/lithos

Research Article

Thermal and decompression history of the Lanzo Massif, northern Italy: Implications for the thermal structure near the lithosphere–asthenosphere boundary

Tomo Aoki [a], Kazuhito Ozawa [a,*], Jean-Louis Bodinier [b], Françoise Boudier [c], Yuto Sato [a]

[a] Department of Earth and Planetary Science, Graduate School of Science, The University of Tokyo, 7-3-1 Hongo, Bunkyo-ku, Tokyo 113-0033, Japan
[b] Geosciences Montpellier, Place Eugène Bataillon, 34090 Montpellier, France
[c] University of Montpellier, Faculté des Sciences de Montpellier, Place E. Bataillon, 34095 Montpellier, France

ARTICLE INFO

Article history:
Received 31 May 2019
Received in revised form 25 June 2020
Accepted 25 June 2020
Available online 5 July 2020

Keywords:
Lithosphere–asthenosphere boundary
Mantle
Plagioclase lherzolite
Thermal structure
Geotherm
Lanzo Massif

ABSTRACT

The lithosphere–asthenosphere boundary (LAB) is a zone where thermal, mechanical, and material interactions take place between the conductive mantle and the underlying convective mantle, and it plays an important role in plate tectonics. In this paper we focus on the thermal aspects of the LAB zone, based on a petrological study of a large peridotite complex that experienced exhumation in the solid state, for the most part. The complex of interest is the Lanzo Massif in the western Alps, northern Italy, where we were able to clarify its thermal and exhumation history and estimate the original thermal structure before exhumation. We examined plagioclase-bearing lherzolites collected from 16 localities, covering the entire massif. All the constituent minerals show compositional heterogeneities on the grain scale. The patterns of Ca, Al, and Cr zoning in pyroxene, the fluorescence-corrected Ca zoning of olivine adjacent to pyroxenes, the Cr and Al zoning of spinel adjacent to plagioclase, and the Ca and Na zoning of plagioclase suggest that an early, nearly isothermal decompression of the Lanzo Massif partly crossing the dry solidus was followed by monotonous cooling through the plagioclase-facies peridotite field. Various deformation microstructures allowed us to specify the timing of the deformation in the framework of the decompression history by carefully observing their relationships with the compositional zoning of the minerals. We show that the deformation took place mainly when effective cooling had started following a period of nearly isothermal exhumation. By applying several geothermometers and evaluating the compositional zoning of the minerals, we were able to quantify the spatial variations in the thermal and decompression history of the Lanzo Massif and constrain the timescales of decompression and cooling. All the estimated temperatures decrease from the southern body towards the northern body. The grain-scale patterns of zoning indicate that the temperatures recorded by the cores of orthopyroxene (1000–1200 °C) indicate a long period of residence in the mantle, whereas those recorded by the rims of pyroxenes and the cores and rims of olivine (600–1100 °C) represent closure temperatures at various times during the decompression. All the closure temperatures decrease from south to north, while the temperature differences between the cores and rims of orthopyroxene increase. This suggests that the cooler and probably shallower northern body cooled at a relatively slow rate than the hotter and probably deeper southern body. The decrease in temperature of ~60 K from south to north, calculated from orthopyroxene cores, may represent the geotherm near the LAB zone. A thermal gradient of ~10 K/km is indicated, which is significantly greater than that estimated for deep subcontinental lithosphere in a steady thermal state. Such a high geotherm might have been caused by thermal perturbation from the underlying hotter asthenospheric mantle.

1. Introduction

The lithosphere–asthenosphere boundary (LAB) is a zone where thermal, mechanical, and material interactions take place between the conductive mantle (lithosphere) and the underlying convective mantle (asthenosphere), and it plays an important role in plate tectonics (Fischer et al., 2010; Kawakatsu and Utada, 2017; McKenzie et al., 2005; Rychert and Shearer, 2009). The LAB zone has been defined in many ways in terms of its seismic, rheological, and thermal properties, but the nature of its defining mechanism remains controversial (Karato, 2012). One of the proposed models for the origin of the LAB invokes partial melting under conditions that are either dry or unspecified

* Corresponding author at: Department of Earth and Planetary Science, Graduate School of Science, The University of Tokyo, 7-3-1 Hongo, Bunkyo-ku, Tokyo 113-0033, Japan
E-mail address: ozawa@eps.s.u-tokyo.ac.jp (K. Ozawa).

https://doi.org/10.1016/j.lithos.2020.105661

(Press, 1959; Ringwood, 1962; Spetzler and Anderson, 1968; Kawakatsu et al., 2009), H_2O-bearing but undersaturated (Lambert and Wyllie, 1970; Niu and Green, 2018), H_2O saturated (Sato and Ozawa, 2019), or H_2O–CO_2 fluid-bearing (Hirschmann, 2010). The other models consider depth variations in whole-rock H_2O content (Hirth and Kohlstedt, 1996; Karato and Jung, 1998), the solubility of H_2O in orthopyroxene (Mierdel et al., 2007), grain size (Faul and Jackson, 2005), and grain-boundary disorder near the melting temperature (premelting; Takei, 2019). The present-day LAB is not accessible for direct observations of its internal structures and the dynamics operating there, observations that would probably have helped clarify the mechanisms of its formation. Nevertheless, large exposures of mantle material exhumed onto the surface of the Earth on a scale greater than a few tens of kilometers, such as orogenic peridotite complexes and ophiolites, may provide important constraints on the structures and processes operating in the LAB zone. In this paper we describe the results of our study of the Lanzo peridotite massif in the western Alps, northern Italy, which provides the opportunity to examine exhumed mantle material that probably represents an ancient LAB. We clarify the variability of the thermal and decompression history of the massif based on a petrological study, and we estimate the thermal structure of this ancient LAB zone.

The Lanzo Massif is one of the largest exposures of mantle material exhumed by the Alpine orogeny during the early Mesozoic (Fig. 1; Nicolas et al., 1972; Boudier, 1978; Nicolas, 1984), and it extends over 150 km^2 including its serpentinized marginal zone. The massif is thought to have been exhumed during the opening of the Jurassic Ligurian–Piedmontese Sea between the European and Adriatic continents, following slow spreading of the Atlantic mid-ocean ridge (Müntener and Piccardo, 2003; Nicolas, 1984; Piccardo et al., 2009). The Lanzo Massif is characterized by MORB-source mantle-like geochemistry (Bodinier, 1988; Bodinier et al., 1991), and it has heterogeneities on various scales (Bodinier, 1988; Bodinier et al., 1991; Guarnieri et al., 2012; Kaczmarek and Müntener, 2010). Heterogeneity on the scale of the massif (~20 km) was reported by Bodinier et al. (1991) and Lorand et al. (1993), who argued that its northern part represents subcontinental lithospheric mantle with high $^{143}Nd/^{144}Nd$ values that was isolated from the convective mantle 400–700 myr ago, while its southern part represents an asthenospheric mantle diapir with $^{143}Nd/^{144}Nd$ ratios in the same range as Atlantic MORB. Kaczmarek and Müntener (2010) argued from smaller-scale (~5 km) heterogeneities that the lithospheric mantle underwent modification by melts derived from the asthenosphere in relation to deformation during exhumation of the massif. Piccardo et al. (2007) and Sanfilippo et al. (2014, 2017) examined the southern part of the Lanzo Massif, particularly the dunite bodies that are predominant in this part of the massif, and they attributed their formation to reaction between the lithospheric mantle and melts derived from the underlying asthenosphere. The massif may represent lithospheric mantle close to the lithosphere–asthenosphere boundary (LAB), or even the LAB zone itself, and as such it can provide information on lithosphere–asthenosphere interactions including a range of magmatic processes. Guarnieri et al. (2012) studied the northern part of the Lanzo Massif and found geochemical contrasts between depleted and enriched lithologies. They argued that the northern part of the massif represents subcontinental lithosphere that was exposed to the sea floor in a marginal position close to the Adriatic continental margin, while the southern part represents extensively melt-modified lithospheric mantle exposed in a more distal setting, in the Ligurian–Piedmontese basin. These previous studies showed that the Lanzo Massif represents an ancient LAB zone exposed on the Earth's surface over a few hundred square kilometers.

Previous studies of the petrology of the Lanzo Massif (e.g., Bodinier, 1988; Bodinier et al., 1991; Boudier and Nicolas, 1972; Jollands and Müntener, 2019; Kaczmarek and Müntener, 2008; Pognante et al., 1985), the results of which are summarized in the Supplementary Material, have raised four important issues concerning temperatures, pressures, and the deformation history of the massif. First, how can we properly apply geothermobarometry to minerals with chemical heterogeneity that developed during the continuous exhumation and cooling of the Lanzo Massif with the possible added complication of partial melting? Second, where did the Lanzo Massif originally reside before it was brought into and cooled through the plagioclase peridotite facies, and which pressure–temperature path did the massif take? Third, is there spatial variability in the history of decompression within the Lanzo Massif? Fourth, when did deformation take place during the exhumation of the massif? The aim of this paper is to address all these issues, but in order to do this, it is important to have a thorough understanding of the chemical heterogeneity and microstructures of the minerals in the massif, as well as their variability within the massif, and to know how those heterogeneities formed in relation to changes in pressure, temperature, and system compositions as well as deformation and partial melting. The strategy we took during our study was therefore to evaluate the chemical heterogeneity and microstructures of the constituent minerals of the massif, and to examine thoroughly the internal variations of these features within the massif.

2. Geological background

The Lanzo Massif consists dominantly of plagioclase-bearing lherzolite, which is stable at pressures lower than 1 GPa, along with subordinate amounts of mafic rock that occurs as layers or dikes (Bodinier, 1988; Bodinier et al., 1991; Boudier, 1976, 1978; Boudier and Nicolas, 1972; Nicolas et al., 1972; Pognante et al., 1985). The massif is divided into the northern, central, and southern bodies on the basis of petrographic characteristics (Boudier, 1978). The peridotite of the northern body is characterized by the replacement of primary minerals by low-temperature secondary minerals such as antigorite, chlorite, and diopside, and previous studies have shown these to have formed during the high-pressure Alpine metamorphism (e.g., Kienast and Pognante, 1988; Pelletier and Müntener, 2006). The widespread occurrence of antigorite as the major serpentine mineral indicates that this metamorphism was distinct from that which took place during the sea-floor exposure of part of the serpentinite envelope of the Lanzo Massif (sea-floor metamorphism; Lagabrielle et al., 1989; Debret et al., 2013). The peridotites in the central body are medium- to coarse-grained while those of the southern body are coarse-grained and include abundant dunite. The peridotites of the central and southern bodies are less serpentinized than those of the northern body, and they are characterized by the presence of lizardite/chrysotile, which might have formed either by sea-floor metamorphism or during the final exhumation of the massif, as suggested by Debret et al. (2013). The northern and central bodies are separated by a high-temperature shear zone, and the central and southern bodies by a low-temperature shear zone (Boudier, 1978). The northern shear zone consists of various strongly deformed rocks with microstructures from porphyroclastic to mylonitic (Boudier, 1978; Kaczmarek and Müntener, 2010). Remarkable foliations, lineations, and mineral lattice- and shape-preferred orientations are also developed in the massif, and these mostly trend NNE–SSW except for those near the northern shear zone (Boudier, 1976, 1978).

3. Samples and analytical methods

We examined 16 plagioclase lherzolite or plagioclase-bearing harzburgite samples, which were taken from localities that covered the entire Lanzo Massif (Table 1; Fig. 1). We did not examine plagioclase-absent depleted rocks such as Cr-rich spinel-bearing harzburgites and dunite because (1) clinopyroxene tends to be absent in these rocks, which means useful thermometry is not applicable; (2) their pyroxenes, if present, are small in grain size, which causes difficulty in accessing high-temperature information that is usually preserved in the cores of large pyroxenes; and (3) they have distinctively different whole-rock chemical compositions (Bodinier, 1988), which

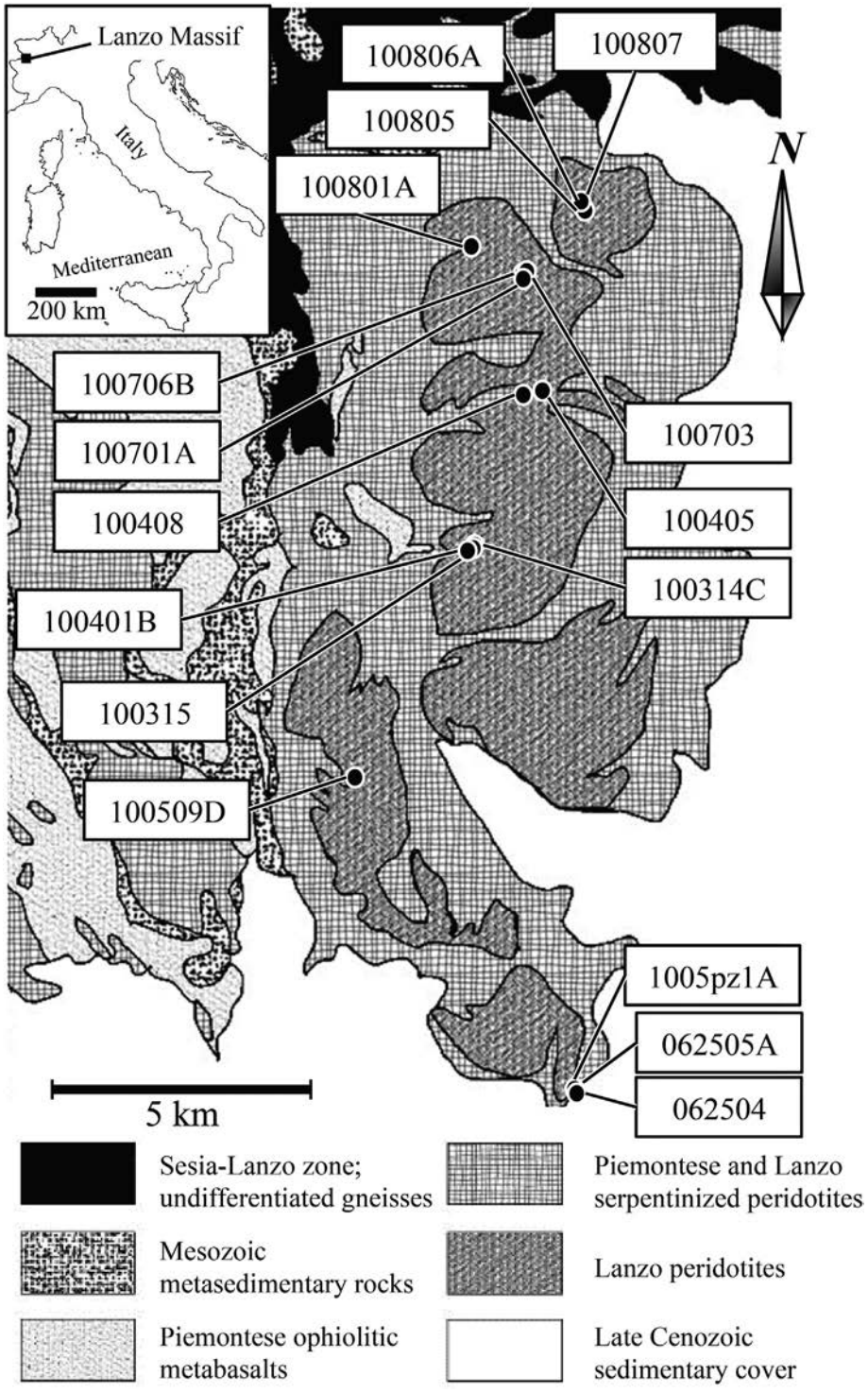

Fig. 1. Geological map of the Lanzo Massif after Boudier (1972, 1976, 1978), showing the locations of samples examined in this study (solid circles with sample numbers).

causes difficulty in examining thermal structures on the scale of the massif, because some thermometers are sensitive to the whole-rock ratios of Mg/(Mg + Fe) (Mg# hereafter) and Cr/(Cr + Al) (Cr# hereafter). Minerals in the samples were analyzed with an electron microprobe analyzer (EPMA) at the University of Tokyo, Tokyo, Japan. Mapping analyses of entire thin sections of several samples were made for five elements (Mg, Al, Ca, Fe, and Cr) in order to examine centimeter-scale chemical heterogeneities, the spatial distribution of minerals, and their modal abundances. The analytical conditions were a 15 kV accelerating voltage, a 120 nA sample current on a Faraday cup, a 30 μm pixel size, and a 60 msec dwell time. For each thin section, mapping analyses of the five elements were performed on the largest grains (1–7 mm in size) under the above conditions with a 1–10 μm pixel size and a 30–45 msec dwell time. Quantitative analyses of eleven elements (Si, Al, Ti, Fe, Mn, Mg, Ca, Na, Cr, Ni, and K) were made under the conditions of a 15 kV accelerating voltage, a 12 nA sample current on a Faraday cup, and three repetitions of 10 s count time at peak and 5 s for background on both sides of the peak. Analyses of Ca in olivine were

Table 1
Modal composition of primary minerals, mean Mg/(Mg + Fe) of olivine, and list of secondary metamorphic minerals for exained plagioclase peridotites.

Unit	Sample	Rock Type	Texture	Ol	Opx	Cpx	Sp	Pl	Others	Mg# of olivine	Secondary phases	Metamorphism
North	100807	Pl lhz	Equigranular	–	–	–	–	–	–	0.884 ± 0.009	Atg, Tr, Chl, mOl, Di, Mag, Slf, Ilm	strong
	100806A	Pl lhz	Protogranular	–	–	–	–	–	–	0.906 ± 0.005	Atg, Tr, Chl, mOl, Di, Mag, Slf, Cb	strong
	100805	Pl lhz	Equigranular	–	–	–	–	–	–	0.893 ± 0.006	Atg, Brs-Wnc, Chl, mOl, Di, Mag, fChr, Slf	strong
Shear zone	100801A	Pl lhz	Protogranular	–	–	–	–	–	–	0.898 ± 0.003	Zo, Grt, Atg, Tr, Chl, Hbl, Di, Slf	Moderate
	100701A#	Pl lhz	Porphyroclatic	58.0	28.2	5.5	0.20	8.1	–	0.903 ± 0.002	Zo, Grt, Chl, Di, Ctl/Lz	Faint
	100703	Pl lhz	Mylonite	–	–	–	–	–	–	0.903 ± 0.001	Zo, Grt, Pg, Chl, Ab, Lab, Ctl/Lz	Faint
	100706B	Pl lhz	Mylonite	–	–	–	–	–	–	0.903 ± 0.001	Zo, Grt, Pg, Chl, Olg, Ctl/Lz, Brc	Faint
Central	100405	Pl hzb	Protogranula	68.4	14.2	4.0	0.24	5.7	7.48	0.896 ± 0.007	Zo, Brs-Wnc, Grs, Jd, Tr, Chl, Di, Atg, fChr, Slf	Moderate
	100408	Pl lhz	Tabular equigranular	69.4	19.3	5.1	0.38	5.9	–	0.902 ± 0.001	Zo, Pg, Chl, Ab, Olg, Andes, Lab, Clt/Lz	Faint
	100401B	Pl lhz	Tabular equigranular	61.1	27.6	4.8	0.57	5.3	0.68	0.907 ± 0.003	Zo, Grt, Grs, Pg, Jd, Tr, Chl, Olg, Clt/Lz	Very weak
	100315	Pl lhz	Protogranular	64.7	14.7	11.3	0.54	8.8	–	0.898 ± 0.001	Zo, Brs-Wnc, Pg, Jd, Chl, Qz, Slf, Omp, Ab, Andes, Clt/Lz	Faint
	100314C#	Pl lhz	Protogranular	63.3*	15.9	6.5	0.07	14.2*	–	0.884 ± 0.015	Zo, Grt, Grs, Pg, Jd, Tr, Chl, Omp, Di, Gln, Qz	Weak
South	100509D	Pl lhz	Protogranular	68.8	14.1	11.7	0.66	4.6	0.18	0.905 ± 0.001	Zo, Grt, Pg, Jd, Tr, Chl, Qz, Ctl/Lz	Faint
	1005pz1A#	Pl lhz	Protogranular	67.6	22.5	5.6	0.16	4.2	–	0.909 ± 0.001	Zo, Pg, Chl, Lab, Ctl/Lz, Tlc	Faint
	062505A#	Pl lhz	Protogranular/Banded	57.3	20.2	13.9	0.13	8.5	–	0.904 ± 0.001	Zo, Pg, Chl, Ab, Andes, Lab, Ctl/Lz	Faint
	062504	Pl lhz	Protogranular	70.4	18.0	5.4	0.58	5.7	–	0.906 ± 0.001	Zo, Grt, Pg, Lab, Chl, Olg, Ctl/Lz, Spn	Faint

Abbreviations: lhz: lherzolite, hzb: harzburgite, Mg#: Mg/(Mg + Fe), Ol: olivine, Opx: orthopyroxene, Cpx: clinopyroxene, Sp: spinel, Pl: plagioclase, Atg: antigorite, Tr: tremolite, Hbl: hornblende, Omp: omphacite, Brs: barroisite, Wnc: winchite, Chl: chlorite, mOl: metamorphic olivine, Di: diopside, Mag: magnetite, Slf: sulfides, Cb: carbonates, fChr: ferrite chromite, Zo: zoisite, Jd: jadeite, Pg: paragonite, Grt: garnet, Grs: grossular, Gln: glaucophane, Ab: albite, Olg: oligoclase, Andes: Andesine, Lab: labradorite, Ctl: chrysotile, Lz: lizardite, Tlc: talc, Brc: brucite, Ilm: ilmenite, Spn: sphene, Qz: quartz. The modal abundances were detemined by point counding and are listed in volume % except for samples marked with #, the modal abundances of which were obtained by EPMA mapping of the entire thin sections. Modal abundance was not determined for mylonitic samples and strongly metamorphosed samples., —: no reliable data because of strong-moderate metamorphism/alteration or deformation, *:a half of metamorphic chlorite rimming plagioclase was counted as plagioclase and the other half as olivine. The sample 100314C is classified as plagioclase lherzolite, though it is mela olivine gabbronorite according to the modal composition if the IUGS classification scheme is strictly followed.

made with a 20 kV accelerating voltage, a 50 nA sample current on a Faraday cup, and a counting time at peak of 100 s and 50 s for background on both sides of the peak. Analyses of CaO in olivine made in the vicinity of clinopyroxene and orthopyroxene were corrected for fluorescence effects by using PENELOPE (Llovet et al., 2005) with the densities of olivine, orthopyroxene, and clinopyroxene taken from Abramson et al. (1997), Chai et al., 1997, and Collins and Brown (1998), respectively.

The mean compositions of mineral cores and rims were obtained to clarify the variations on the scale of the massif (~20 km). Line analyses of pyroxenes were obtained for grains that were mapped to obtain representative positions for the lines profiles. The analytical conditions were the same as those for the analyses of mean compositions except for a beam size of 20 μm, which may have provided bulk pyroxene compositions that included the fine exsolution lamellae, if the lamellae were thinner than ~1 μm. The line chemical analyses of pyroxenes were made across grains in a direction perpendicular to the exsolution lamellae. For representative mineral compositions of cores and rims, analyses of 5–10 points for rims and 20–40 points for cores were averaged.

4. Petrography

Photomicrographs of representative samples from the three bodies of the Lanzo Massif and the northern shear zone are shown in Figs. 2 and 3. The dominant minerals in the plagioclase-bearing peridotites are olivine, orthopyroxene, clinopyroxene, plagioclase, and spinel (Table 1), which we will call "primary minerals" as distinct from "secondary minerals" that formed during either sea-floor metamorphism or the Alpine high-pressure metamorphism (Debret et al., 2013; Kienast and Pognante, 1988; Pelletier and Müntener, 2006). The primary pyroxenes and plagioclases are distributed heterogeneously on the scale of a thin section in some samples (Fig. S13). Most of the samples contain more than 5 modal% of clinopyroxene, and can be classified as lherzolite except for one sample (100405, 4.0% clinopyroxene; Table 1; Fig. S14). The amount of plagioclase is mostly 4–6 modal%, but it reaches 8–9 modal% in three samples and 14 modal% in one sample that shows a heterogeneous distribution of the plagioclase (Fig. S13b–d). The modal% of plagioclase and the modal ratio of spinel/(spinel + plagioclase) show a negative correlation (Table 1; Fig. S15).

Secondary minerals such as the serpentine minerals, chlorite, tremolite, diopside, zoisite, jadeite, and paragonite replace primary minerals or fill veins or veinlets that cut across the primary minerals in varying degrees (Table 1). The secondary phases are minor in samples from the central and southern bodies and the northern shear zone, and they are limited to the replacement of olivine and orthopyroxene by serpentine (lizardite and/or chrysotile) and of plagioclase by very fine-grained mineral aggregates (saussurite pseudomorphs after plagioclase; Fig. 2b–d and f–h). The pseudomorphs after plagioclase consist mostly of chlorite in the northern body and of fine-grained (a few to several tens of microns) aggregates of zoisite, jadeite, paragonite, and a more sodic plagioclase, garnet (grossular and almandine), and other minor phases in the other parts of the massif (Table 1; Fig. S11). The metamorphic minerals making up the saussurite are consistent with those described by Debret et al. (2013), though paragonite is also observed in our samples, especially in the southern body (Table 1; Fig. S11d–h). Jadeite intergrown with zoisite in the saussurite is restricted to the central body and the northern part of the southern body (Table 1; Fig. S11e and f), and the assemblage jadeite–quartz is found only in the vicinity of the boundary between the central and southern bodies (Table 1). Secondary phases are abundant in samples from the northern body, and they include antigorite as a serpentine mineral, aggregates of diopside and tremolite replacing orthopyroxene, tremolite replacing clinopyroxene, chlorite replacing plagioclase, and ferritchromite and magnetite replacing spinel (Table 1; Fig. 2a and e). The plagioclase and spinel in our samples from the northern body have been almost completely replaced by secondary phases.

The grain size of olivine in the peridotites tends to increase from the northern body (~0.5–1.0 mm) through the central body to the southern body (~1–2 mm) (cf. Fig. 22a, c, and d), as reported by Boudier and Nicolas (1977), but with the exception of the northern shear zone (0.01–0.10 mm; Fig. 2b and f; Kaczmarek and Müntener, 2008). Orthopyroxenes are larger (4–6 mm maximum size) than the olivines

and clinopyroxenes (1–3 mm maximum size). Plagioclase and spinel generally tend to occur as isolated grains, but local concentrations of each define lineations and foliations in the central and southern bodies (Fig. 2g and h; Fig. S13b–d). Large irregularly shaped grains of spinel mostly have rims of plagioclase, and this is always the case in the shear zone and northern body (Fig. 2e and f; Fig. S13a) where the spinel grains are always elongate and aligned parallel to the lineation and foliation. The plagioclase rims around spinel grains in the northern shear zone accentuate the lineation and foliation, as they tend to develop in the direction of the spinel elongation as polycrystalline aggregates and are thin or even absent in the direction perpendicular to foliation (Fig. 2e and f).

In all samples, very thin exsolution lamellae of clinopyroxene are generally homogeneously developed in large orthopyroxene grains (Fig. 3b–d). Exceptions are near the grain margins, where the lamellae tend to be thinner, low in number density or even absent, and along tilt boundaries, where the lamellae are thicker and lower in number density. Short lamellae of clinopyroxene, oblique to the homogeneously distributed long lamellae, are present sporadically in the centers of large orthopyroxenes (Fig. 3d).

Exsolution lamellae of orthopyroxene are developed in the clinopyroxenes, and they are thicker than the clinopyroxene lamellae in the orthopyroxenes (Fig. 3e–h). They are of consistent thickness and distributed homogeneously except near the margins, where the lamellae tend to become thinner, low in number density, or even absent. Elongate patches of orthopyroxene 10–50 μm in thickness are observed near the centers of large clinopyroxene grains (Fig. 3h). This patchy orthopyroxene is in the same topotaxic relationship with the host clinopyroxene as the thin exsolution lamellae. The thin, long orthopyroxene exsolution lamellae become thinner around the patchy orthopyroxene, lower in number density, or even absent. As also reported by Kaczmarek and Müntener (2008), large clinopyroxene grains have a strongly indented morphology (Fig. 3e, g, and h), and the concavities tend to be filled with orthopyroxene and plagioclase, with the former on the inside (Fig. 3h).

5. Mineral compositions

All the constituent minerals of the rocks of the Lanzo Massif show compositional zoning on the grain scale. In Fig. 4 we present X-ray maps of Al, Ca, and Cr in one of the largest orthopyroxene grains for each unit of the Lanzo Massif (the northern, central, and southern bodies, and the northern shear zone) and we present line profiles of Al_2O_3 and CaO in Fig. 5 and Cr_2O_3 contents and Cr# values in Fig. 6. The same data for one of the largest clinopyroxene grains in each unit of the massif are presented in Fig. 7 (X-ray maps) and Figs. 8 and 9 (line profiles). The same data for the second largest grains of orthopyroxene and clinopyroxene are presented as the Supplementary Material in Figs. S1–S6. Line profiles of the TiO_2 contents in two of the largest orthopyroxenes and clinopyroxenes are presented in Figs. S7 and S8.

The heterogeneities of Ca contents in olivine grains near their contacts with pyroxene are presented as line profiles in Fig. 10, and the relationships between CaO contents and Mg# values in olivine rims in contact with pyroxene are presented as the Supplementary Material in Fig. S9. The heterogeneous contents of Cr in spinel are shown in the X-ray map in Fig. 11a, and those of Ca in plagioclase in Fig. 11b. The mean compositions of the constituent minerals in representative samples from each unit of the massif are listed in Table 2. The spatial variations of these mean values are plotted in Fig. 12.

6. Chemical zoning

6.1. Orthopyroxene

The Al in the orthopyroxenes consistently shows patterns of concentric zoning in X-ray maps with contents monotonously and smoothly decreasing from the cores to the rims irrespective of grain size and location in the massif (Figs. 4a–d and S1e–h). The profiles of Al in large orthopyroxene grains (Figs. 5a–d and S1a–d) clearly show that they do not have a flat core region and are bell-shaped, even for grains as large as 6 mm. This is consistent with the profiles of Al in orthopyroxenes up to ~5 mm in size in peridotites from the northern shear zone, as described by Kaczmarek and Müntener (2008) and Jollands and Müntener (2019).

The X-ray maps of Ca in large orthopyroxene grains show the numerous exsolution lamellae of clinopyroxene that are distributed homogeneously except near grain margins where they are low in abundance or absent (Figs. 3b–d, 4e–h, and S2e–h). The distribution of Ca shows a few high-Ca bands that are highly oblique to the clinopyroxene exsolution lamellae (e.g., Fig. 4f–h), and these bands are due to the presence of tilt boundaries, along which the clinopyroxene lamellae become thicker, shorter, and lower in number density than those away from the bands. The high-Ca bands are associated with zones of low Ca on both sides (e.g., Fig. 4f and h), and they appear as faint bands in X-ray maps of Al without disturbing the concentric patterns of Al zoning (cf. Fig. 4b–d and f–h).

The Ca profiles in the orthopyroxenes show patterns with noisy variations, even after taking running averages, which is due to the presence of clinopyroxene exsolution lamellae (Fig. 5e–h). It is notable that the Ca profiles have consistent core regions, if the spikes where tilt boundaries are crossed are ignored, and that the Ca contents decrease steeply in the marginal zones towards the outermost rims. Therefore, all the Ca profiles show trapezoidal patterns with flat plateaux combined with sharp drops in marginal zones. Such patterns contrast with those of Al, which are smooth and bell-shaped with only minor disturbances (Fig. 5a–d).

The Cr contents in the large orthopyroxene grains of the Lanzo Massif consistently show concentric zoning with sharp decreases in the marginal zones towards the outermost rims (Figs. 4i–l and S3i–l). The patterns in the internal regions of the orthopyroxenes are either nearly flat or show a weak decrease in intensity towards grain centers. The Cr profiles in orthopyroxene grains (Fig. 6a–d) reflect such a two-dimensional Cr distribution, and they are characterized by trapezoidal patterns that are slightly depressed in the core regions or M-shaped with marginal humps (Fig. 6a–d). Many of the Cr zoning profiles reported by Jollands and Müntener (2019) from the northern shear zone fall into two groups: one is similar to the Cr zoning pattern with marginal hump (1/3 of the profiles) while the other is characterized by a simple decrease from the cores to the rims (2/3 of the profiles). The profiles of Cr# values are, however, all smoothly concave upwards without any flat cores (Fig. 6e–h), and this contrasts with the Cr profiles, which have marginal humps in some grains but nearly flat core regions in others (Fig. 6e–h cf. Fig. 6a–d). Orthopyroxenes from the Lanzo Massif show a distinct zoning in TiO_2 contents, characterized by increases from the cores to the rims without any flat core regions (Fig. S7).

6.2. Clinopyroxene

The distribution of Al in X-ray maps of the large clinopyroxene grains shows generally concentric patterns, with monotonous decreases in Al from the cores to the rims irrespective of grain size or location in the Lanzo Massif (Figs. 7a–d and S4e–h). The mostly concentric zoning of Al in two dimensions has maximum contents in the morphological centers of grains (Figs. 4a and c and S4e–h), but the concentric Al zoning pattern of some grains is breached by indentations of the grain boundary with the Al depletion zone narrower than where the rim was not breached (Fig. 7b and d). The thickness of the zone of Al depletion near the margins is therefore variable, but it is thicker where the grain boundary is convex outwards and thinner where it is convex inwards (Fig. 7b and d). The X-ray intensity maps and concentration profiles for Al in large clinopyroxene grains (Figs. 7a–d and 8a–d) clearly show that no profiles have a flat core region, even for grains as large as

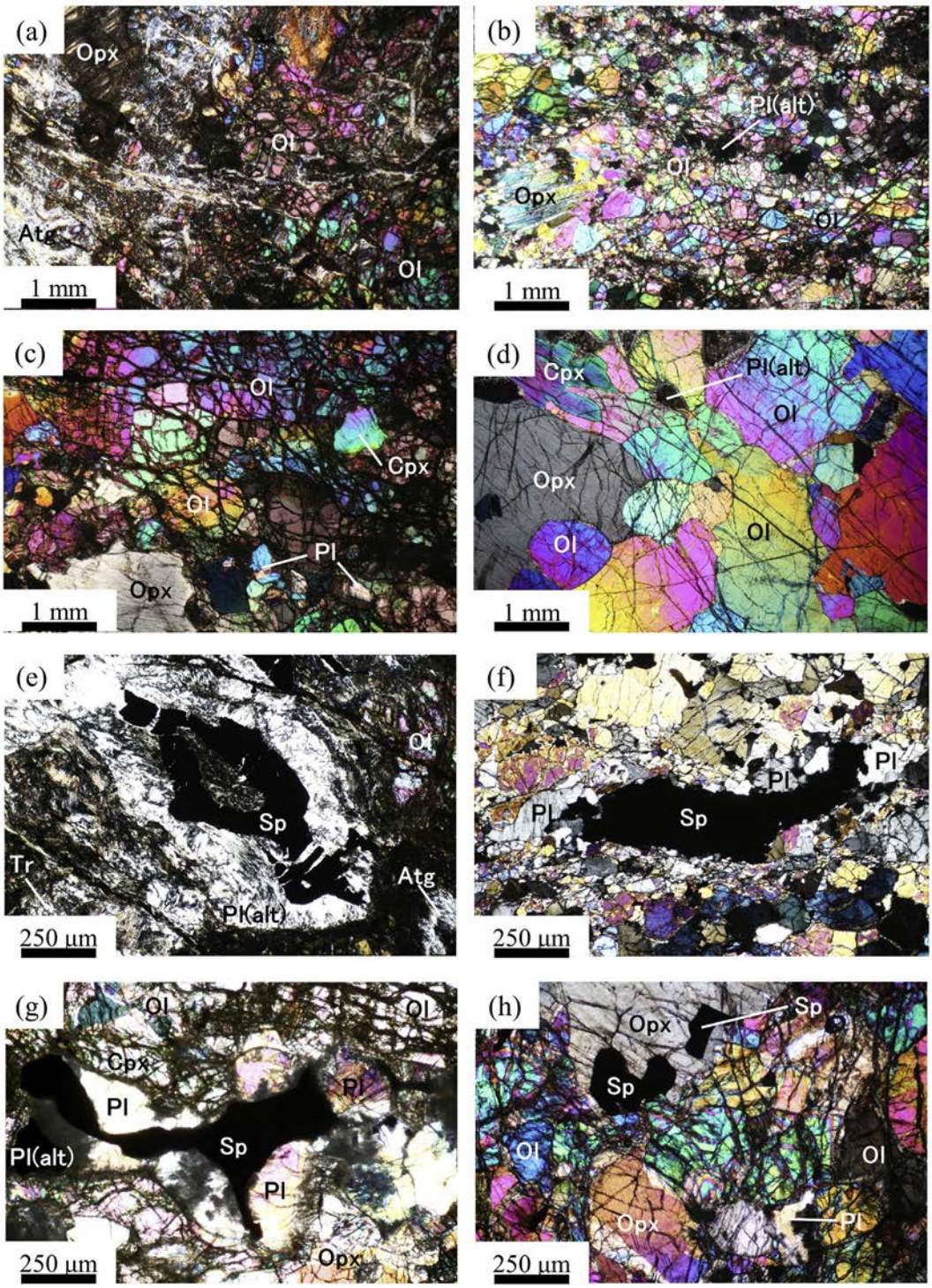

Fig. 2. Photomicrographs of representative microstructures of olivine and other phases observed under crossed polarized light. (a) Medium-grained olivine (Ol) and orthopyroxene (Opx) partially replaced by antigorite (Ant) and other secondary phases in sample 100807 from the northern body. (b) Fine-grained olivine, orthopyroxene (Opx), and completely saussuritized plagioclase (Pl (alt)) in porphyroclastic peridotite from the shear zone (100701A). (c) Medium-grained olivine, orthopyroxene, clinopyroxene (Cpx), and plagioclase (Pl) in peridotite from the central body (100408). (d) Coarse-grained olivine and pyroxenes showing a protogranular texture in peridotite from the southern body (100509D). (e) Anhedral spinel grain surrounded by plagioclase that is completely replaced by chlorite (Pl(alt)), set in olivine partially replaced by antigorite in sample 100807 from the northern body. (f) Anhedral elongate spinel grain surrounded by polycrystalline plagioclase in sample 100801A from the northern sear zone. The relevant Cr and Ca maps are shown in Fig. 11. (g) Anhedral spinel grain associated with partially altered plagioclase in specimen 100408 from the central body. (h) Partially altered plagioclase isolated from subhedral spinel that occurs along the margins of orthopyroxene in specimen 062504 from the southern body.

3 mm, though the patterns of zoning are flatter than those of Al in the orthopyroxenes.

The regularly spaced exsolution lamellae of orthopyroxene are identifiable in the X-ray maps for Al (Figs. 7a–d and S4e–h). Large clinopyroxene grains have orthopyroxene patches near the grain centers (Figs. 3h and 7b and d), and these patches are shorter and thicker than the regularly spaced orthopyroxene lamellae, but they have the same extinction position, which indicates a topotaxic

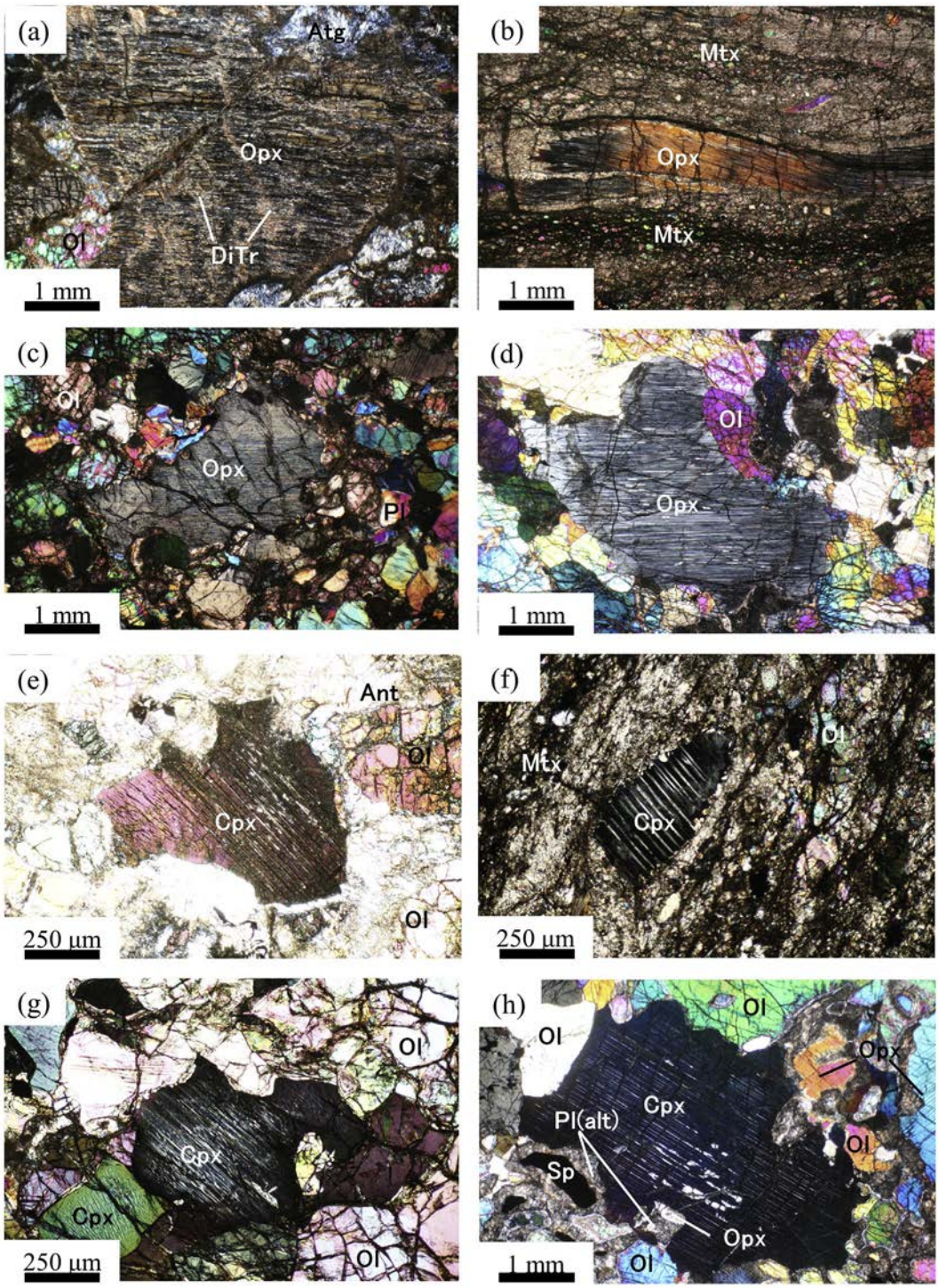

Fig. 3. Photomicrographs of representative microstructures of pyroxenes observed under crossed polarized light. (a) Large orthopyroxene grain (Opx) extensively replaced by secondary minerals (DiTr; fine aggregate of tremolite and diopside) and surrounded by olivine (Ol) partially replaced by antigorite (Ant) in peridotite from the northern body (100807). (b) Strongly deformed orthopyroxene porphyroclast with numerous thin, undulating clinopyroxene exsolution lamellae that are set in a very fine-grained matrix (Mtx) of peridotite mylonite from the northern shear zone (100706B). (c) Large orthopyroxene grain with numerous thin clinopyroxene exsolution lamellae, set in a finer matrix of medium-grained olivine and plagioclase (Pl) in peridotite from the central body (100408). (d) Large orthopyroxene grain with numerous clinopyroxene exsolution lamellae of two morphological types: homogeneously distributed, abundant, thin, long types, and minor, short, thick types that are localized in the grain center. The grain is set in a coarse-grained olivine-rich matrix of peridotite from the southern body (062504). (e) Large clinopyroxene grain with regularly spaced orthopyroxene exsolution lamellae surrounded by olivine partially replaced by antigorite in peridotite from the northern body (100807). (f) Clinopyroxene porphyroclast with regularly spaced orthopyroxene exsolution lamellae in peridotite mylonite from the northern shear zone (100706). The clinopyroxene is set in a fine-grained matrix. (g) Large clinopyroxene grain in peridotite from the central body (100408), which contains many regularly spaced orthopyroxene exsolution lamellae, thinning out towards the margin. (h) Large clinopyroxene grain in peridotite from the southern body (100509D), showing two types of orthopyroxene exsolution lamellae: abundant, thin, long, regularly spaced types and localized thick, short, patchy types.

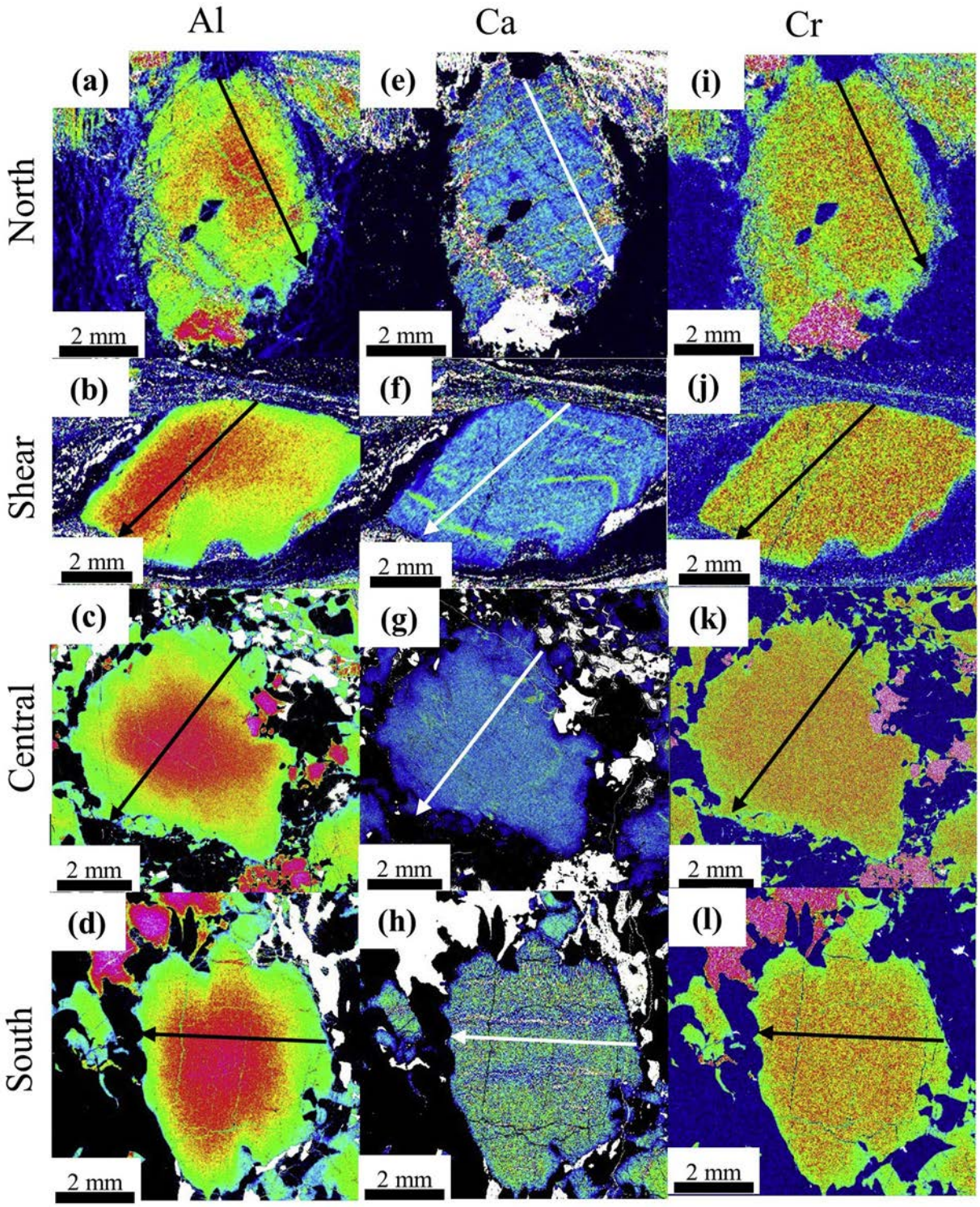

Fig. 4. X-ray pseudo-color intensity maps of Al (a–d), Ca (e–h), and Cr (i-l) for one of the largest orthopyroxene grains in each examined unit: the northern, central, and southern bodies, and the northern shear zone. The orthopyroxene grains show a remarkable gradual decrease in Al from the cores to the rims (a–d). The Ca X-ray maps (e–h) show the development of clinopyroxene exsolution lamellae (light blue–green fine striations) and the depletion of Ca accompanied by a sharp decrease in the number density of the clinopyroxene exsolution lamellae in the marginal zones of the grains. In the Cr X-ray maps (i–l), the orthopyroxene grains consistently show a concentric pattern of zoning with sharply decreasing concentrations in the marginal zone towards the outermost rim, with or without a central weak depression. The black and white lines with arrowheads indicate the positions of the line profiles shown in Figs. 5 and 6.

relationship with the host clinopyroxene. The patchy topotaxic orthopyroxene is present exclusively in the Al-rich portions of the clinopyroxenes invaded by the grain boundary (Fig. 7b and d).

The X-ray maps of Ca in the large clinopyroxenes show mostly concentric patterns of zoning with high-Ca margins and flat core regions where many low-Ca orthopyroxene lamellae are present (Figs. 7e–h and S5e–h). The orthopyroxene lamellae are regularly spaced but thicker in the grain centers, and they become thinner, fewer, or even absent in the marginal zones. The profiles of Ca in the clinopyroxenes show noisy variations due to the presence of orthopyroxene exsolution

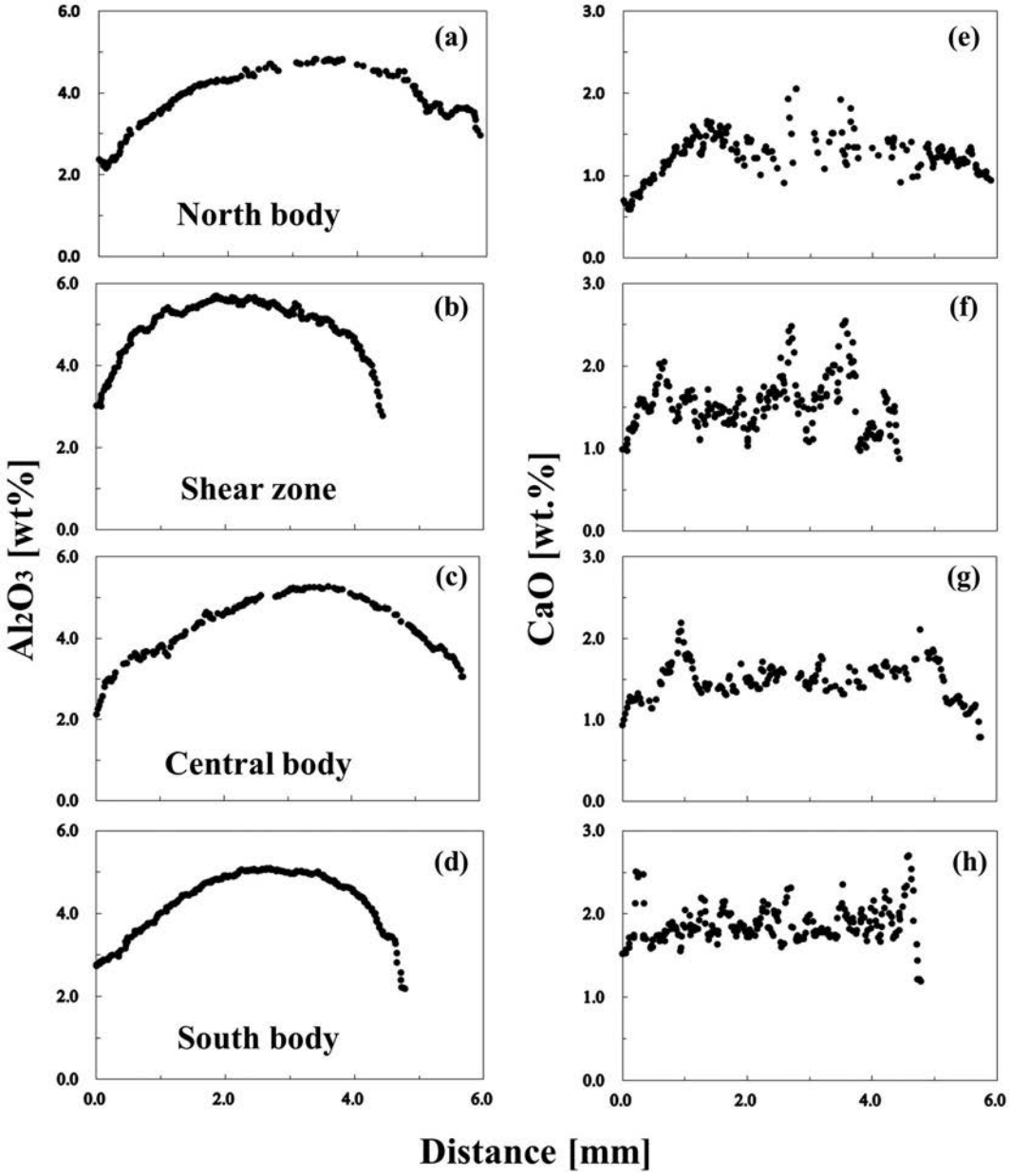

Fig. 5. Line profiles of Al_2O_3 wt% (a–d) and CaO wt% (e–h) for one of the largest orthopyroxene grains in each examined unit (the northern, central, and southern bodies, and the northern shear zone), shown as the five-point moving average. The locations of profiles for (a)–(h) are shown on Fig. 4a–h. The analyses were made with a broad beam (20 μm in size). Each line profile in two dimensions starts from a rim and goes through the grain center to the rim on the other side of the grain. The scattered distributions above or below the mean concentrations in the CaO profiles are due to the presence of thicker exsolution lamellae of clinopyroxene, mostly along tilt boundaries.

lamellae, which are much thicker than the clinopyroxene lamellae in the orthopyroxenes (Fig. 8e–h). There is, however, a consistent core region, if spikes due to the presence of thick orthopyroxene lamellae or patches are ignored, and the Ca contents sharply increase towards the rims from these core regions (Fig. 8e–h). All the profiles therefore show inverted trapezoidal patterns with flat bottoms and sharp increases in the marginal zones.

The X-ray maps of Cr in large clinopyroxene grains consistently show concentric zoning patterns characterized by gradual decreases of Cr towards the grain centers, and mostly without flat core regions (Figs. 7i–l and S6i–l). The Cr mostly increases towards the outermost rims, but some grains show a local decrease in Cr towards their rims (Fig. 7j and l), which is most distinct where grain surfaces thinly protrude (Fig. 7j). The profiles of Cr in clinopyroxene grains reflect the two-dimensional distribution of Cr, and they are characterized by a concave upwards pattern (Fig. 9b and c). The decrease in Cr in the outermost rim noticed in the Cr maps is seen only in the Cr profile of Fig. 9d, and this is because the beam size (20 μm) adopted for measuring the profiles for Fig. 9 was almost the same as the width of the zone with the sharp decrease. The profiles of Cr# values are all smoothly concave upwards without any flat cores, and they show remarkable increases towards the outermost rims (Fig. 9e–h). The clinopyroxenes in the Lanzo Massif show a distinct zoning in TiO_2, with increases from the cores to the rims and no flat core regions (Fig. S8).

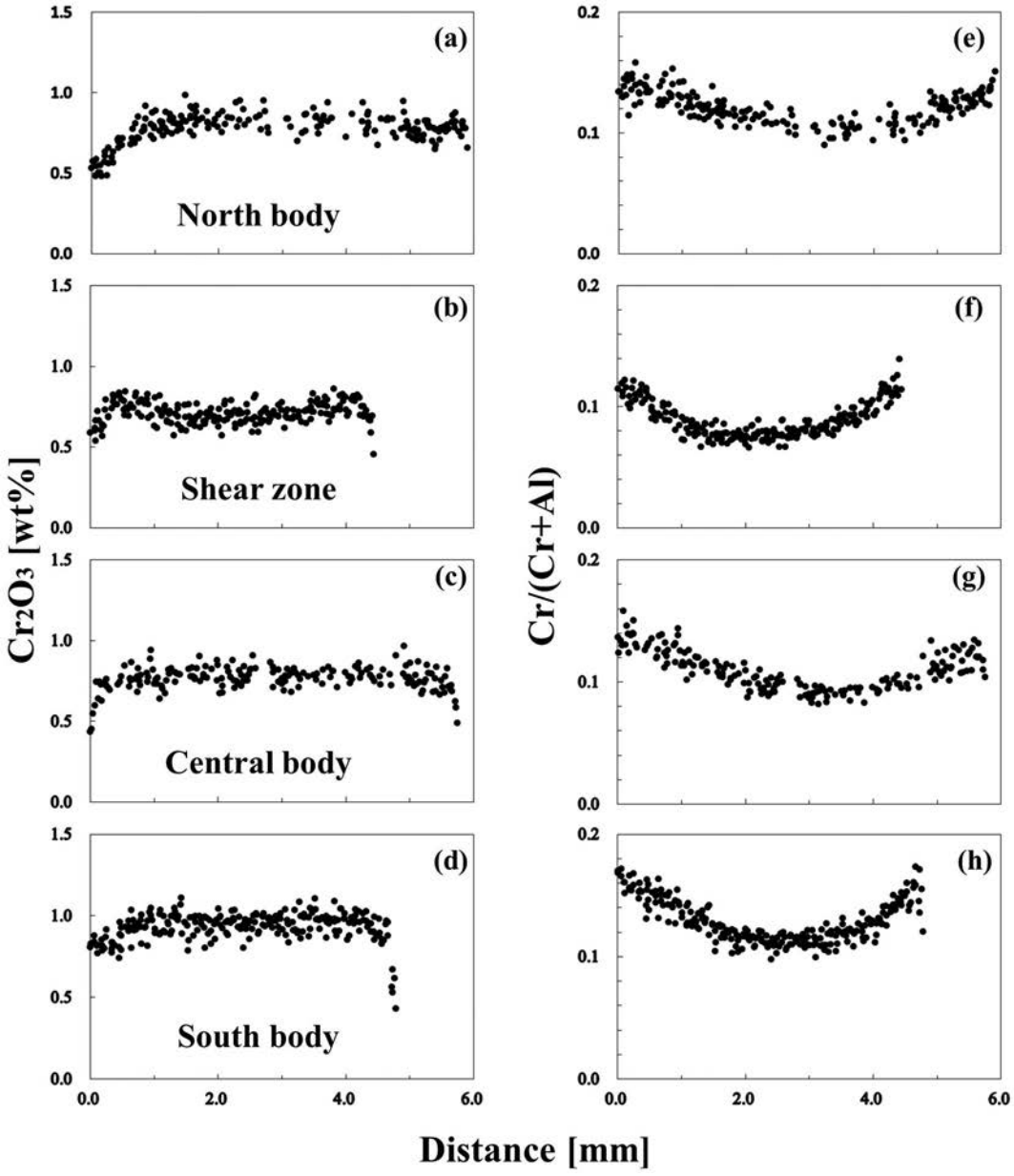

Fig. 6. Line profiles of Cr_2O_3 wt% (a–d) and Cr/(Cr + Al) cation ratios (e–h) for one of the largest orthopyroxene grains in each unit: the northern, central, and southern bodies, and the northern shear zone. The locations of the profiles are shown on Fig. 4i-l. The analyses were made with a broad beam (20 μm in size). Each line profile in two dimensions starts from a rim and goes through the grain center to the rim on the other side of the grain.

6.3. Olivine

The Mg# values for the olivines in the Lanzo Massif range from 0.88 to 0.91 (Table 1), which is within the range reported by others (Boudier, 1978; Kaczmarek and Müntener, 2008; Pognante et al., 1985). Fluorescence-corrected Ca profiles for the olivines towards their contacts with pyroxenes are shown in Fig. 10. Because of the low concentrations, the profiles are fairly scattered and not smooth, particularly for olivines from the northern body and the shear zone, where the overall Ca concentrations are low. However, there is a clear pattern characterized by a monotonous decrease from the flat cores towards the rims over distances of up to 0.5 mm, except in the olivines from the shear zone, which are polycrystalline with a grain size of ~10–100 μm (Fig. 10). The decreasing trend of Ca towards the rims is also confirmed by the Ca-intensity maps of several samples, even if the fluorescence effect is taken into consideration. The profiles towards pyroxene contacts are similar for clinopyroxene or orthopyroxene.

6.4. Spinel

The mean Cr# values for spinels in the Lanzo Massif range from 0.2 to 0.7 (Table 2), which is within the range reported by others (Boudier, 1978; Kaczmarek and Müntener, 2008; Pognante et al., 1985). Spinels show an overall enrichment in Cr and depletion in Al towards their rims, though they show notable heterogeneities in the Cr# values within each grain, as reported by Kaczmarek and Müntener (2008) (Fig. 11a). The zoning is characterized by the coexistence of several local Cr maxima (Al minima) and Cr minima (Al maxima) on the interfaces with surrounding minerals, usually plagioclase. The local Cr maxima tend to occur on grain surfaces that are parallel or slightly oblique to the foliation plane (yellow-red-white colored parts in Fig. 11a). In contrast, the local Al maxima tend to occur where the spinel grain morphology is concave outwards, which is in the direction of the lineation or close to this direction (Fig. 11a). The intimate relationship between Al or Cr

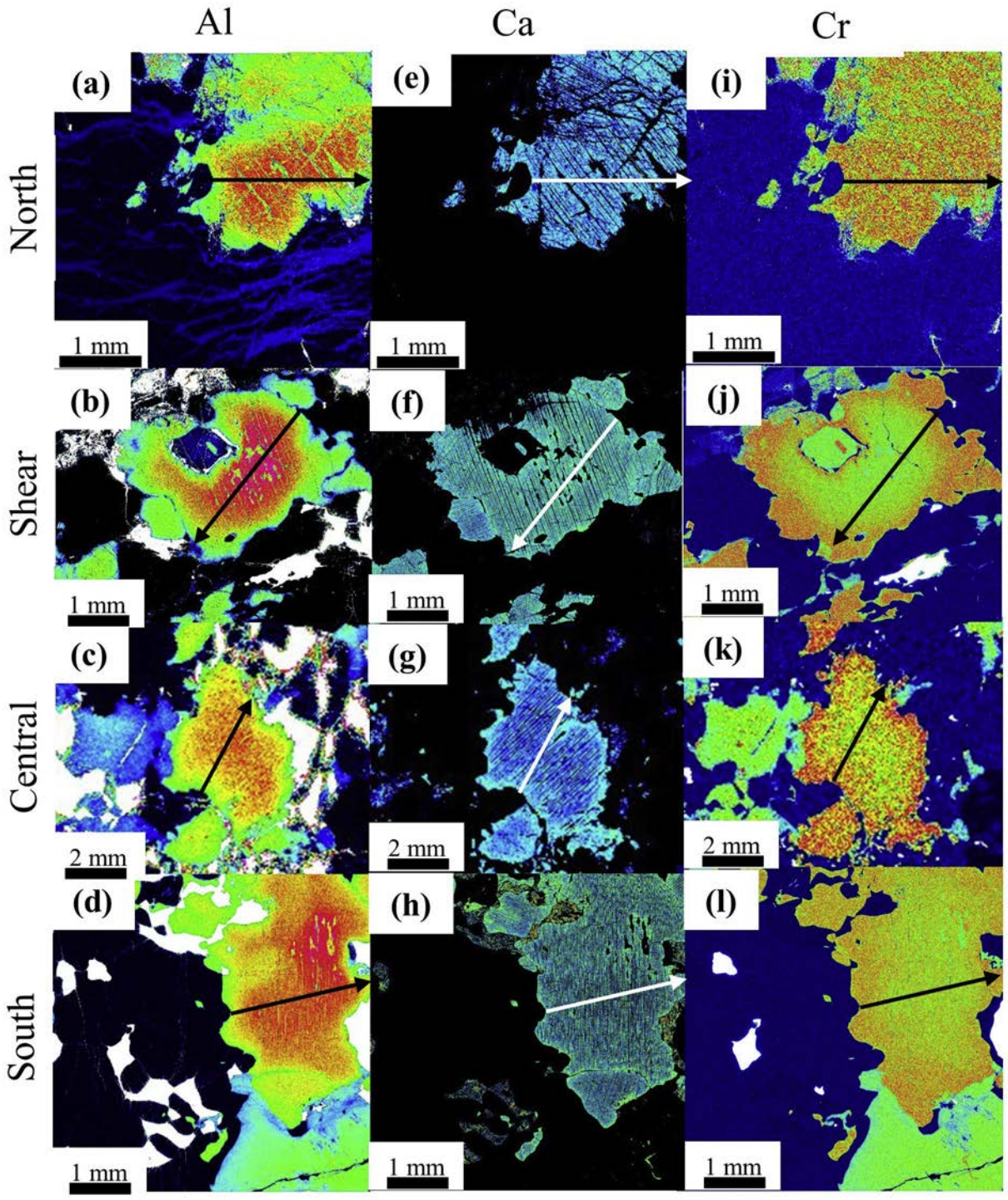

Fig. 7. X-ray pseudo-color intensity maps for Al (a–d), Ca (e–h), and Cr (i-l) in one of the largest clinopyroxene grains for each unit: the northern, central, and southern bodies, and the northern shear zone. The clinopyroxene grains show a continuous decrease in Al from the cores to the rims (a–d) and an enrichment in Ca accompanied by the thinning and disappearance of orthopyroxene exsolution lamellae in the marginal zones (e–h). The Cr X-ray maps consistently show a concentric pattern of zoning and a notable increase in Cr towards the margins and a very sharp decrease towards the outermost rims (i–l). The black and white lines with arrowheads indicate the positions of the line profiles shown in Figs. 8 and 9.

enrichment and spinel morphology is consistent with that observed by Kaczmarek and Müntener (2008).

6.5. Plagioclase

The values of Ca/(Ca + Na), or An contents hereafter, in the plagioclases of the Lanzo Massif, range from 0.7 to 0.9 (Table 2), which is within the range reported by others (Boudier, 1978; Pognante et al., 1985; Kaczmarek and Müntener, 2006). Most plagioclase grains in our samples have been replaced at least partly by fine-grained aggregates of secondary minerals, and the EPMA analyses of plagioclase are therefore limited to samples 100408, 100703, 062505A, and 062504. The An contents of plagioclases that rim spinel increase remarkably towards their contacts with spinel from ~0.75 to ~0.90, and increase moderately

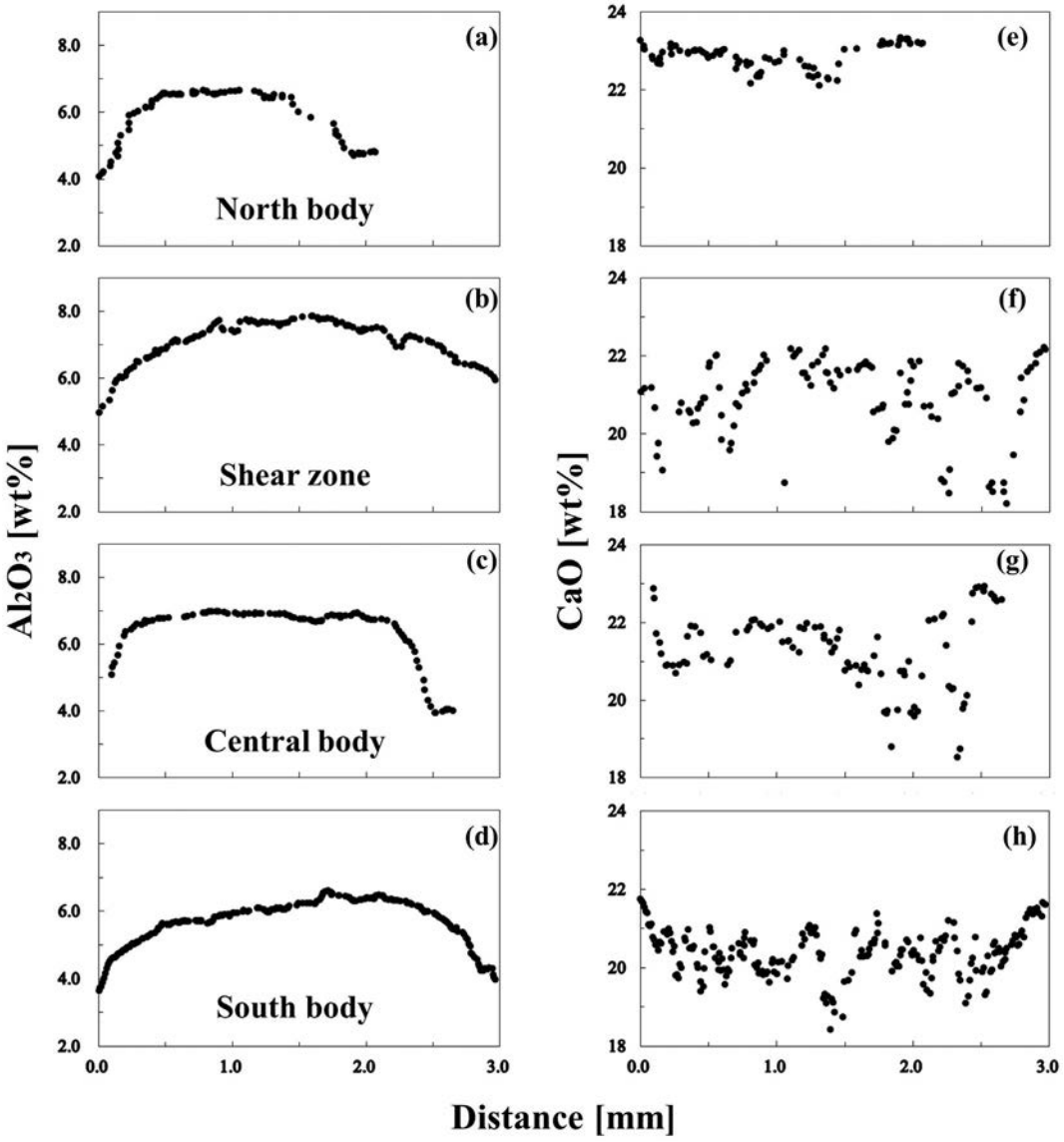

Fig. 8. Line profiles of Al_2O_3 wt% (a–d) and CaO wt% (e–h) for one of the largest clinopyroxene grains in each unit (the northern, central, and southern bodies, and the northern shear zone), shown as the five-point moving average. The locations of the profiles (a–h) are shown on Fig. 7a–h. The analyses were made with a broad beam (20 μm in size). Each line profile in two dimensions starts from a rim and goes through the grain center to the rim on the other side of the grain. The scattered distributions below or above the mean concentrations in the CaO profiles are due to the presence of thick exsolution lamellae of orthopyroxene.

towards polycrystalline plagioclase grain boundaries from ~0.75 to ~0.80, particularly towards plagioclase–plagioclase grain boundaries that are highly oblique to the lineation (yellow–red colored parts in Fig. 11b). Plagioclase grains that are isolated from spinel and form aggregates in the central and southern bodies show a relatively weak concentric zoning of Ca with An contents increasing from ~0.72 to ~0.77 towards the rim of each plagioclase grain ("reverse An zoning"; Ozawa and Takahashi, 1995). The highest An content in each rock is found at the rims of plagioclase in contact with spinel.

7. Variations in the compositions of pyroxenes and olivine on the scale of the massif

The mean concentrations of CaO in the cores of orthopyroxenes tend to decrease in the massif as a whole from south to north (Fig. 12a), with 1.81–1.96 wt% in the southern body and 1.31–1.49 wt% in the northern body (Table 2). The grain sizes of the examined orthopyroxenes range from 2.0 to 6.0 mm, and there is no spatial variation in the massif (Fig. 13b). The mean CaO contents of the rims are distinctly lower than those of the cores, and they tend to decrease from south to north, with 1.32–1.64 wt% in the southern body and 0.87–1.25 wt% in the northern body. The widths of strongly zoned margins with minor exsolution lamellae of clinopyroxene tend to increase from south to north (Fig. 13a), and they are ~0.2 mm in the southern body and ~ 1.0 mm in the northern body. The Al_2O_3 contents of the cores and rims of orthopyroxenes in the Lanzo Massif range from 4.0 to 6.0 wt% and 2.0 to 3.0 wt%, respectively (Fig. 5a–d), but there is no clear systematic spatial variation.

The mean concentrations of CaO in the cores of the clinopyroxenes tend to increase from south to north (Fig. 12b), with ~20–21 wt% in the southern body and ~ 22–23 wt% in the northern body (Table 2). The maximum grain size of the examined clinopyroxenes ranges from 0.05 to 3.5 mm, and there is no spatial variation within the massif (Fig. 13b). The mean CaO contents in the clinopyroxene rims are distinctly higher than those of the cores, and they tend to increase from south to north (Fig. 12b; Table 2), with ~22 wt% in the southern body and ~ 23 wt% in the northern body. The Al_2O_3 contents of the clinopyroxene cores and rims range from 6.0 to 8.0 wt% and 4.0 to

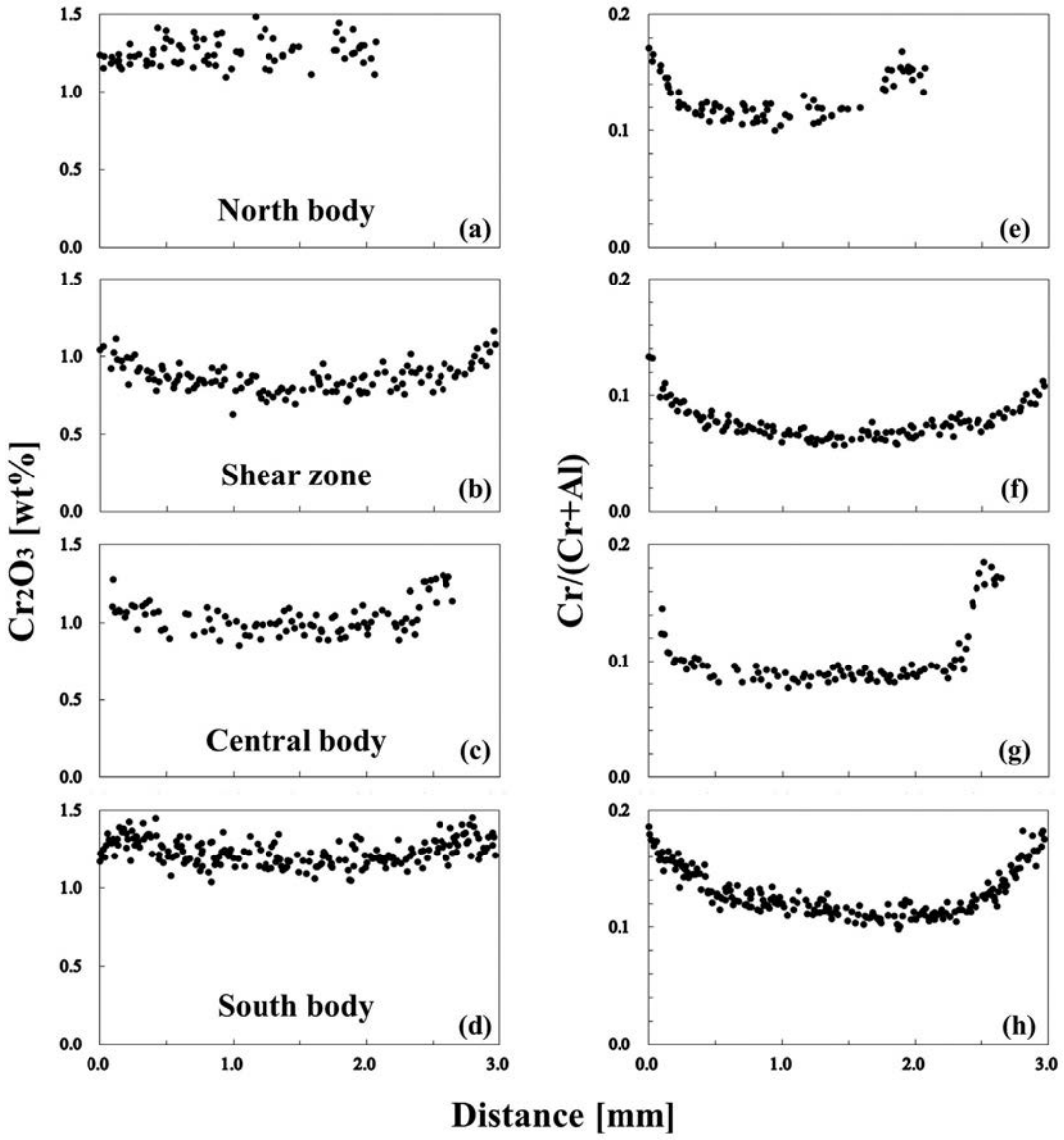

Fig. 9. Line profiles of Cr_2O_3 wt% (a–d) and Cr/(Cr + Al) cation ratios (e–h) for one of the largest clinopyroxene grains in each unit: the northern, central, and southern bodies, and the northern shear zone. The locations of profiles are shown on Fig. 7i–l. The analyses were made with a broad beam (20 μm in size). Each line profile in two dimensions starts from a rim and goes through the grain center to the rim on the other side of the grain.

5.5 wt%, respectively (Fig. 8a–d), but there is no clear systematic spatial variation.

There is a systematic spatial variation of the CaO contents of olivine in the Lanzo Massif, as shown in Figs. 10 and 12c. The CaO contents of olivine cores tend to decrease from south to north (Fig. 12c; Table 2), with ~0.05–0.09 wt% in the southern body and ~ 0.02–0.04 wt% in the northern body. The mean CaO contents of the rims are distinctly lower than those of the cores, and they tend to decrease from south to north (Fig. 12c; Table 2) with ~0.02–0.04 wt% in the southern body and < 0.01 wt% in the northern body. The Mg# values of olivine cores tend to decrease from south to north (Fig. 12d), and the values for the rims also tend to decrease from south to north. The differences in the Mg# values of the cores and rims become more pronounced in the northern body than in the southern body.

8. Discussion

All the minerals in the peridotites of the Lanzo complex show notable heterogeneities, which complicates the application of geothermometry. First, therefore, it is necessary to clarify the processes responsible for the zoning in the minerals and their textures (exsolution lamellae, and the topotaxic patches in the pyroxenes) in order to infer a plausible exhumation history that involved cooling and deformation. This clarification is necessary before we can know what the temperatures calculated by geothermometry represent: are they "equilibrium" conditions for prolonged residence in the mantel or those frozen during exhumation accompanied by cooling ("closure temperatures", see below). Clarification of the processes is particularly necessary when a pair of minerals is used for geothermometry, which requires selection of chemical compositions that approached "equilibrium". We therefore apply the geothermometry only after the zoning of the minerals has been thoroughly examined.

8.1. Interpretation of the mineral chemical zoning

The following are some important thermodynamic and kinetic factors that may produce heterogeneities in minerals. (1) The temperature and pressure dependencies of Al solubility in pyroxene in the

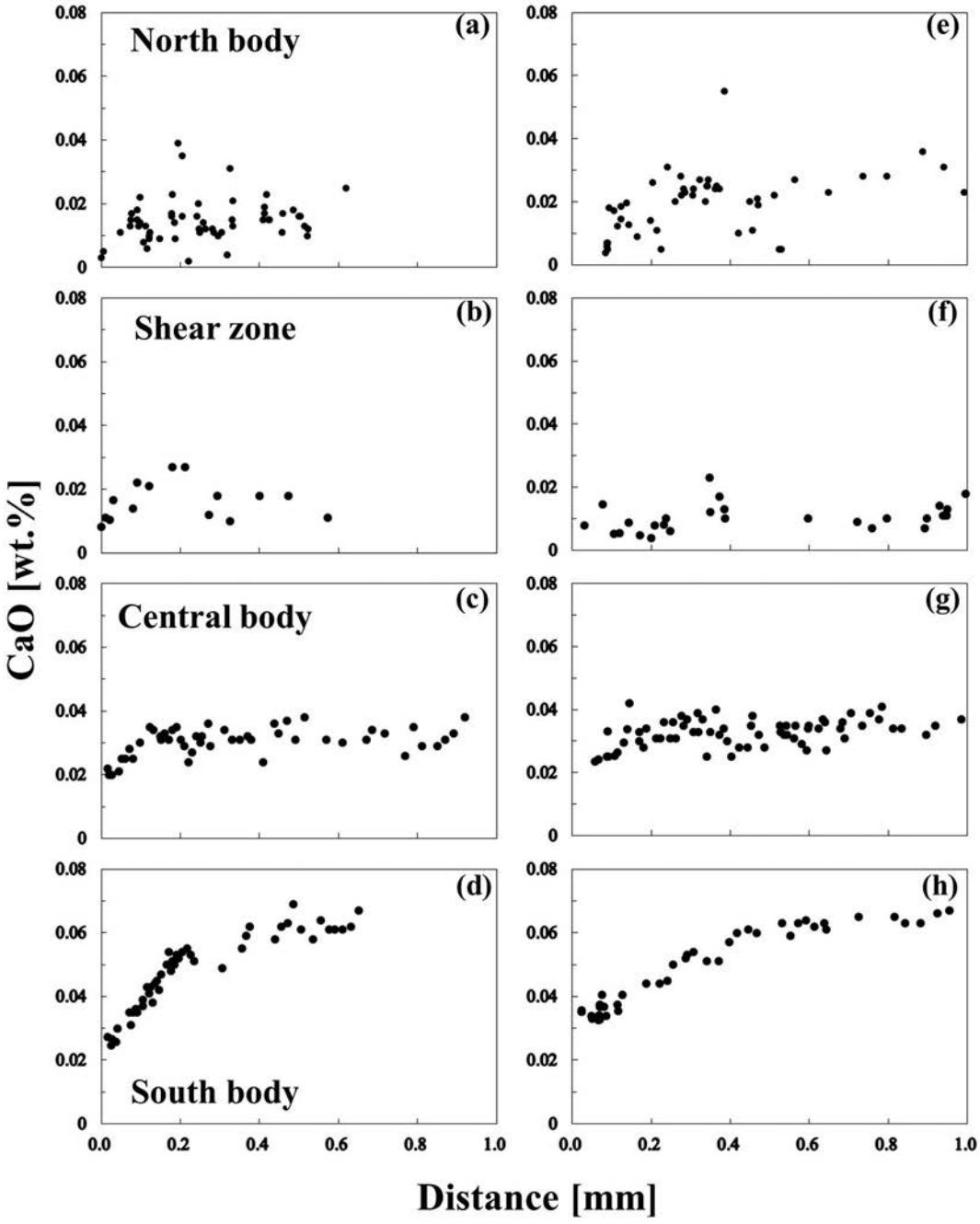

Fig. 10. Line profiles of fluorescence-corrected CaO wt% in olivine adjacent to orthopyroxene (a–d) and clinopyroxene (e–h). Each profile, except for those for samples from the northern shear zone, is for a single olivine crystal starting from the contact with pyroxenes and ending at the core of the olivine where the CaO distribution is nearly homogeneous. The line profiles for the shear zone samples extend over several olivine grains due to the extensive deformation and recrystallization of the olivine. The analyses were made using the instrument settings specific for olivine as described in the text.

plagioclase peridotite facies, which is characterized by strongly negative isopleths on a pressure–temperature diagram (Borghini et al., 2010, 2011; Gasparik, 1984; Obata, 1976). (2) For any given Cr# value in spinel, Cr is more soluble in pyroxenes at higher temperatures irrespective of whether the conditions are of the plagioclase, spinel, or garnet peridotite facies (Borghini et al., 2010; Klemme and O'Neill, 2000; Nagata et al., 1983), and there is an increase in the solubility of Cr in pyroxenes with pressures less than 1 GPa (Borghini et al., 2010) and a decrease in the solubility of Cr in orthopyroxene with pressures greater than 2 GPa (Klemme and O'Neill, 2000), which implies that the pressure and temperature dependencies of Cr solubility in the pyroxenes are essentially the same as those of Al (Obata, 1976). (3) The strongly temperature-dependent mutual solubility of two pyroxenes (Lindsley, 1983). (4) The stronger temperature dependence of orthopyroxene components in clinopyroxene than of clinopyroxene components in orthopyroxene (Lindsley, 1983). (5) The much lower diffusivity of Al and Cr than Ca in pyroxenes (Chakraborty, 2010; Cherniak and Dimanov, 2010; Ganguly et al., 2007; Smith and Barron, 1991). (6) The lower diffusivities of Al, Cr, and Ca in clinopyroxene than in orthopyroxene (Ozawa and Takahashi, 1995). (7) The extremely slow interdiffusion of the anorthite and albite components in plagioclase, which means that the An content of plagioclase is not modified by diffusion once the plagioclase has crystallized (Cherniak, 2010; Grove et al., 1984). (8) The stress/strain induced Al and Cr zoning in spinel (Ozawa, 1989).

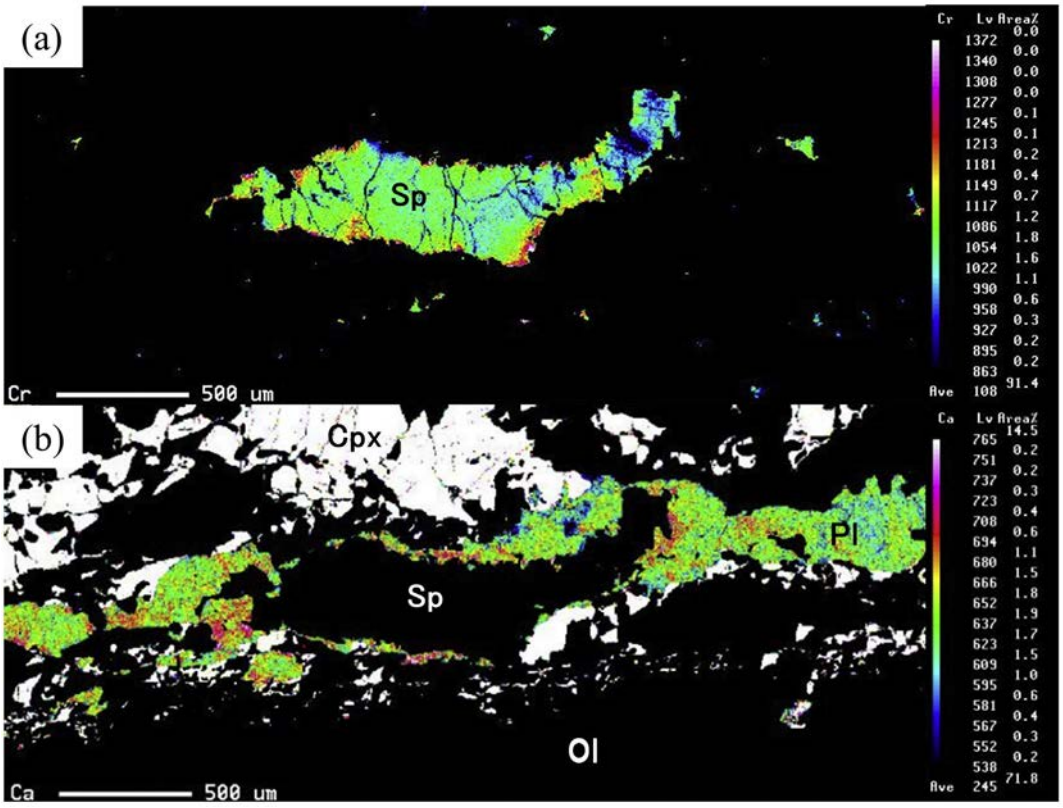

Fig. 11. X-ray pseudo-color intensity maps for Cr in spinel (a) and Ca in plagioclase (b) in sample 100703 from the northern shear zone. The mapped area includes part of the area shown in Fig. 2f. The spinel grain in (a) is surrounded by the plagioclase depicted in (b) and shows several Cr and Al concentration maxima coexisting along the grain boundary. The polycrystalline plagioclase surrounding the spinel grain in (a) shows an increase in Ca towards its grain boundaries that are at high angles to the lineation and the interfaces with spinel. The numbers besides the color bars for each panel are X-ray intensities (count/s) and area%.

We first clarify the origins of the zoning observed in spinel and plagioclase, which is important before examining the zoning in pyroxenes. The occurrence of plagioclase as isolated grains and as plagioclase-rich lenses, pods, and veinlets (Boudier and Nicolas, 1972) indicates that the plagioclase crystallized from an interstitial melt involved in open-system reactions (Guarnieri et al., 2012; Müntener and Piccardo, 2003; Piccardo et al., 2007). On the other hand, the plagioclase that rims spinel and the negative Eu anomaly in the clinopyroxene of the plagioclase lherzolites and pyroxenites suggest the plagioclase crystallized under the strong influence of solid-state reactions such as pyroxenes + spinel = olivine + plagioclase ("secondary recrystallization"; Bodinier et al., 1991; Guarnieri et al., 2012). We have several lines of evidence for the subsolidus origin of some plagioclase: (1) the increase in An towards the rims of plagioclase grains irrespective of its mode of occurrence ("reverse An zoning"; Ozawa and Takahashi, 1995), (2) the extreme enrichment of An at the rims of plagioclase in direct contact with spinel, (3) the selective enrichment of An in the plagioclase rims that lie in the direction of the lineation, (4) the overall increase of Cr# values from the cores to the rims of spinel grains rimmed by plagioclase. The features of plagioclase zoning (1–3 above) and spinel zoning (4) can be attributed to the growth of plagioclase by solid-state reactions under decompression accompanied by deformation (Borghini et al., 2010, 2011; Fumagalli et al., 2017; Gasparik, 2003). The growth of plagioclase is a requisite because the diffusion of Ca in plagioclase is extremely slow (Grove et al., 1984) and the chemical composition could not have been modified by lattice diffusion once fixed at the rim. The role of deformation is also supported by the coexistence of Cr maxima and Al minima on the spinel rims that are aligned parallel to the foliation, and the Cr minima and Al maxima on the rims that are highly oblique to the lineation. We infer from the above, therefore, that plagioclase in the Lanzo Massif may have crystallized from a melt at an early stage, and that its growth continued by solid-state reactions at a later stage during decompression and deformation, at least in the southern and central bodies, where it was possible to examine the chemical zoning of the plagioclase.

The zoning of Al in orthopyroxene (<6 mm in size) and clinopyroxene (<3 mm in size) described above (Figs. 4a–d, 7a–d, S1e–h, and S4e–h) is characterized by a monotonous decrease in Al from cores to rims, no flat core region, and a steepening slope towards the outermost rims. The patterns of zoning are more distinct in the orthopyroxenes, which show more of a bell-shaped zoning pattern than the clinopyroxenes, and some large grains of clinopyroxene have a narrow flat core region where there are orthopyroxene patches. The patterns of Al zoning suggest that there was a continuous decrease of Al at the rims during decompression, with the continuation of this decompression being reflected in the plagioclase zoning (as discussed above) at temperatures higher than those where the reactions involving diffusional loss of Al from the pyroxenes ceased.

The patterns of Cr zoning in the orthopyroxenes are M-shaped with variations in the degree of development of the central depression (Fig. 6a–d) whereas the patterns in the clinopyroxenes are either M- (Fig. 9d) or cup-shaped (Fig. 9a–c). Since the temperature and pressure dependencies of Cr solubility in pyroxene are similar to those of Al, the fact that there are differences in the patterns of Al and Cr zoning (bell-shaped vs. cup- or M-shaped) in the spinel and plagioclase peridotite facies (see the important thermodynamic and kinetic factor (2) above) implies that in addition to changes in pressure and temperature, there were also changes in the Al and Cr budget of coexisting phases. The most plausible explanation is the availability of Cr due to the formation of plagioclase consuming spinel, as indicated by the observed intimate

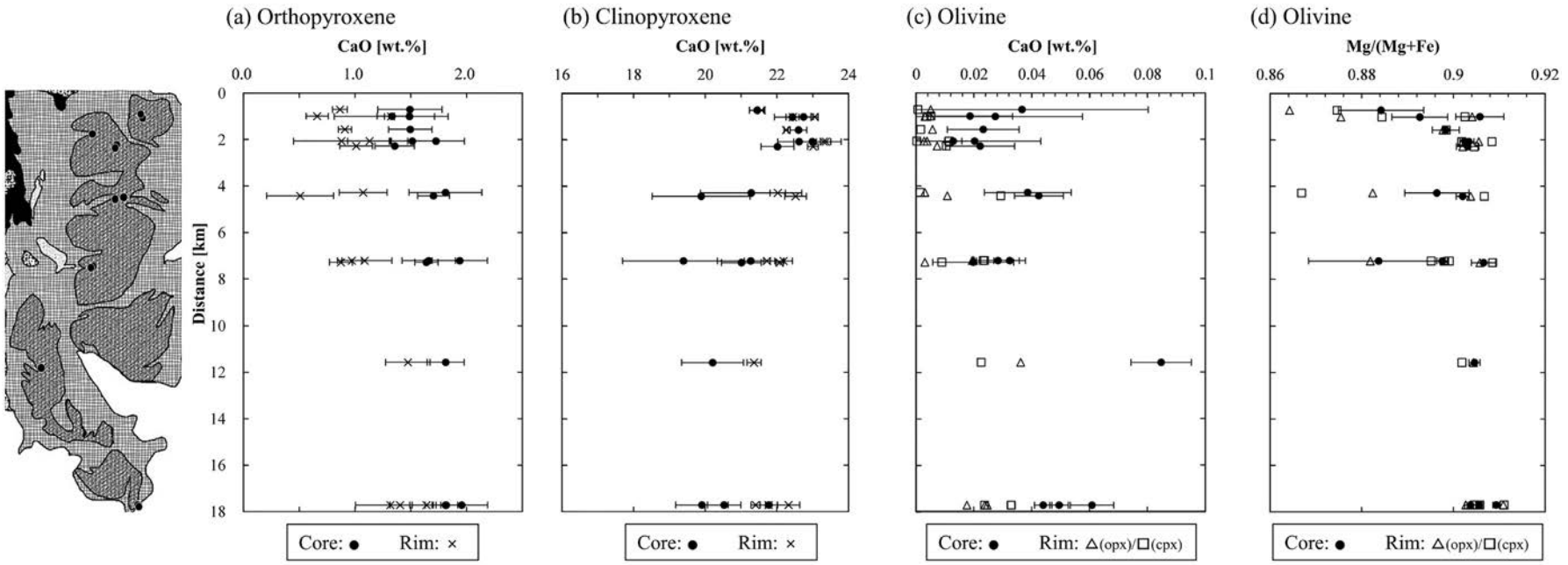

Fig. 12. Spatial variations in the CaO contents of orthopyroxene (a), clinopyroxene (b), and olivine (c), and the Mg/(Mg + Fe) values of olivine (d) in the Lanzo Massif. In each panel, the mean contents of the cores (solid circles) and rims (crosses for pyroxenes, open triangles for olivine in contact with orthopyroxene, and open squares for olivine in contact with clinopyroxene) are plotted with an error of $\pm 1\sigma$. The vertical axes represent the distance measured from the northern end of the massif along a N—S line by projecting along the E–W direction.

Table 2
Mean major element concentrations of constituent minerals in selected plagioclase peridotite from each unit (north, central, and south bodies, and shear zone) in the Lanzo massif with standard deiation (±1 s). -: not analyzed or below the detection limit.

Unit	North body																	
Sample	100806A																	
Mineral	Orthopyroxene						Clinopyroxene						Olivine			Spinel		
Position	Core			Rim			Core			Rim			Core			Core		
(wt%)																		
SiO_2	55.33	±	0.18	56.90	±	0.33	51.11	±	0.20	52.54	±	0.23	41.09	±	0.20	0.02	±	0.01
TiO_2	0.12	±	0.02	0.11	±	0.02	0.36	±	0.03	0.39	±	0.04		–		0.36	±	0.03
Al_2O_3	4.50	±	0.21	2.29	±	0.16	6.57	±	0.12	4.23	±	0.20		–		28.02	±	0.82
Cr_2O_3	0.84	±	0.06	0.53	±	0.04	1.26	±	0.09	1.21	±	0.03		–		34.54	±	0.89
FeO	5.39	±	0.13	5.50	±	0.09	2.69	±	0.12	2.54	±	0.17	9.29	±	0.49	23.03	±	0.25
Fe_2O_3		–			–			–			–			–		3.52	±	0.25
MgO	32.95	±	0.34	34.68	±	0.15	15.44	±	0.46	16.42	±	0.23	50.09	±	0.49	8.26	±	0.30
CaO	1.41	±	0.39	0.66	±	0.10	22.68	±	0.61	23.05	±	0.36	0.02	±	0.01	0.02	±	0.02
MnO	0.13	±	0.02	0.14	±	0.02	0.09	±	0.02	0.07	±	0.01	0.16	±	0.01	0.45	±	0.02
NiO	0.09	±	0.02	0.08	±	0.01	0.05	±	0.02	0.04	±	0.01	0.37	±	0.01	0.15	±	0.02
Na_2O	0.04	±	0.02	0.01	±	0.01	0.67	±	0.04	0.59	±	0.02	–			0.01	±	0.01
K_2O		–			–			–			–			–			–	

UNIT	Shear zone																				
Sample	100703A																				
Mineral	Orthopyroxene						Clinopyroxene						Olivine			Spinel			Plagioclase		
Position	Core			Rim			Core			Rim			Core			Core			Core			Rim		
(wt%)																								
SiO_2	54.43	±	0.24	55.99	±	0.75	51.23	±	0.27	52.25	±	0.38	40.93	±	0.10	0.03	±	0.01	49.13	±	0.31	48.84	±	0.06
TiO_2	0.23	±	0.03	0.21	±	0.04	0.77	±	0.05	0.84	±	0.04		–		0.81	±	0.55		–			–	
Al_2O_3	4.55	±	0.19	2.45	±	0.68	6.02	±	0.11	4.24	±	0.26		–		32.44	±	0.53	32.10	±	0.19	31.76	±	2.03
Cr_2O_3	0.75	±	0.06	0.45	±	0.16	1.05	±	0.05	1.00	±	0.10		–		29.49	±	0.17	0.03	±	0.03	0.07	±	0.00
FeO	6.00	±	0.15	6.07	±	0.03	3.27	±	0.25	2.92	±	0.08	9.55	±	0.10	15.27	±	0.54	0.08	±	0.04	0.27	±	0.14
Fe_2O_3		–			–			–			–			–		5.75	±	0.56		–			–	
MgO	31.79	±	0.43	33.29	±	0.70	15.51	±	1.05	15.75	±	0.22	49.61	±	0.17	14.13	±	0.17	0.01	±	0.01	0.97	±	1.37
CaO	1.62	±	0.56	0.88	±	0.43	22.45	±	1.30	23.36	±	0.18	0.02	±	0.02	0.01	±	0.01	15.27	±	0.21	15.44	±	0.03
MnO	0.15	±	0.02	0.16	±	0.02	0.09	±	0.02	0.09	±	0.02	0.15	±	0.01	0.22	±	0.02	0.01	±	0.01		–	
NiO	0.09	±	0.02	0.09	±	0.02	0.04	±	0.02	0.05	±	0.02	0.33	±	0.005	0.25	±	0.01	0.02	±	0.03	0.01	±	0.01
Na_2O	0.05	±	0.03	0.02	±	0.01	0.67	±	0.06	0.62	±	0.05		–		0.01	±	0.01	2.78	±	0.15	2.31	±	0.15
K_2O		–			–			–			–			–			–		0.01	±	0.01	0.04	±	0.01

Unit	Central body																				
Sample	100408																				
Mineral	Orthopyroxene						Clinopyroxene						Olivine			Spinel			Plagioclase		
Position	Core			Rim			Core			Rim			Core			Core			Core			Rim		
(wt%)																								
SiO_2	55.32	±	0.15	55.65	±	0.76	50.68	±	0.45	51.50	±	0.35	40.85	±	0.07	0.02	±	0.02	50.15	±	0.25	49.11	±	0.14
TiO_2	0.26	±	0.02	0.41	±	0.33	0.61	±	0.06	0.80	±	0.12		–		0.64	±	0.07		–			–	
Al_2O_3	4.24	±	0.08	1.94	±	0.31	6.77	±	0.14	4.26	±	0.40		–		32.08	±	0.67	31.40	±	0.16	32.38	±	0.21
Cr_2O_3	0.78	±	0.06	0.35	±	0.11	0.97	±	0.06	1.08	±	0.12		–		30.76	±	0.68	0.03	±	0.03		–	
FeO	5.54	±	0.12	6.06	±	0.39	3.85	±	0.48	3.07	±	0.28	9.77	±	0.15	14.94	±	0.37	0.13	±	0.05	0.21	±	0.04
Fe_2O_3		–			–			–			–			–		5.35	±	0.43		–			–	
MgO	32.23	±	0.22	34.32	±	0.35	17.38	±	1.96	16.60	±	0.49	50.44	±	0.11	14.23	±	0.32	0.02	±	0.01	0.02	±	0.01
CaO	1.71	±	0.24	0.64	±	0.15	19.75	±	2.70	22.52	±	0.86	0.04	±	0.01	0.01	±	0.01	14.38	±	0.15	15.35	±	0.42
MnO	0.15	±	0.01	0.17	±	0.02	0.12	±	0.02	0.08	±	0.01	0.15	±	0.005	0.23	±	0.02	0.01	±	0.01		–	
NiO	0.09	±	0.02	0.09	±	0.02	0.05	±	0.02	0.05	±	0.02	0.35	±	0.003	0.23	±	0.01	0.02	±	0.03	0.01	±	0.01
Na_2O	0.05	±	0.01	0.01	±	0.01	0.51	±	0.08	0.51	±	0.06		–		0.01	±	0.01	3.26	±	0.08	2.66	±	0.26
K_2O		–			–			–			–			–			–		0.01	±	0.02	0.01	±	0.00

Unit	South body																	
Sample	100509D																	
Mineral	Orthopyroxene						Clinopyroxene						Olivine			Spinel		
Position	Core			Rim			Core			Rim			Core			Core		
(wt%)																		
SiO_2	55.45	±	0.19	56.27	±	0.25	51.47	±	0.28	52.56	±	0.34	40.80	±	0.12	0.02	±	0.02
TiO_2	0.22	±	0.02	0.23	±	0.02	0.46	±	0.04	0.51	±	0.03		–		0.71	±	0.07
Al_2O_3	3.88	±	0.11	2.65	±	0.13	6.18	±	0.21	3.78	±	0.21		–		29.10	±	3.71
Cr_2O_3	0.92	±	0.06	0.68	±	0.08	1.18	±	0.07	1.21	±	0.03		–		36.29	±	2.65

(continued on next page)

Table 2 (*continued*)

Unit	South body																	
Sample	100509D																	
Mineral	Orthopyroxene						Clinopyroxene						Olivine			Spinel		
Position	Core			Rim			Core			Rim			Core			Core		
(wt%)																		
FeO	6.20	±	0.12	6.21	±	0.11	3.64	±	0.28	3.24	±	0.10	9.68	±	0.06	15.76	±	2.04
Fe_2O_3		–			–			–			–			–		3.89	±	0.48
MgO	32.63	±	0.35	33.37	±	0.33	17.18	±	0.85	17.47	±	0.16	49.89	±	0.23	13.82	±	1.74
CaO	1.81	±	0.37	1.47	±	0.20	20.18	±	1.55	21.66	±	0.27	0.09	±	0.003		–	
MnO	0.15	±	0.02	0.16	±	0.02	0.11	±	0.02	0.11	±	0.01	0.15	±	0.01	0.17	±	0.07
NiO	0.10	±	0.02	0.09	±	0.01	0.06	±	0.02	0.04	±	0.01	0.36	±	0.002	0.17	±	0.03
Na_2O	0.03	±	0.02	0.02	±	0.01	0.38	±	0.04	0.37	±	0.03		–		0.01	±	0.01
K_2O		–			–			–			–			–			–	

spatial association of plagioclase and spinel as well as the Ca enrichment of plagioclase and the overall Cr enrichment of spinel grains towards their rims (Borghini et al., 2010, 2011). This is clearly shown by the cup-shaped zoning patterns of Cr# in the pyroxenes, which indicate that Cr was more available than Al during the progress of exhumation (Borghini et al., 2010). The Al and Cr zoning patterns of the pyroxenes were thus formed during the formation of plagioclase from spinel during a process of continuous decompression. The increase in TiO_2 contents from the cores to rims in both orthopyroxene and clinopyroxene can also be attributed to the decomposition of spinel, as suggested by Kaczmarek and Müntener (2008) (Figs. S7 and S8). The sharp drop in Cr that is common in the orthopyroxene (Fig. 6a–d) but rare in the clinopyroxene (Fig. 9d) can be explained more by the effects of temperature decrease rather than the decomposition of spinel during the final stages of exhumation and the slower diffusion of Cr in clinopyroxene than in orthopyroxene.

The patterns of Ca zoning in the pyroxenes, after smoothing the profiles for the effects of exsolution lamellae, are characterized by wide flat core regions and steep decreases in Ca contents towards the rims for the orthopyroxenes but steep increases towards the rims for the clinopyroxenes. The homogeneity of the core regions is consistent with the homogeneous distribution of relatively thin exsolution lamellae in the orthopyroxenes, and the thicker but regularly spaced exsolution lamellae in the clinopyroxenes, with the only exception of the patchy orthopyroxene in some large clinopyroxene grains.

The patterns of zoning in the plagioclase, spinel, and the two types of pyroxene record a process of continuous decompression and cooling, as discussed above. However, the details of the decompression path

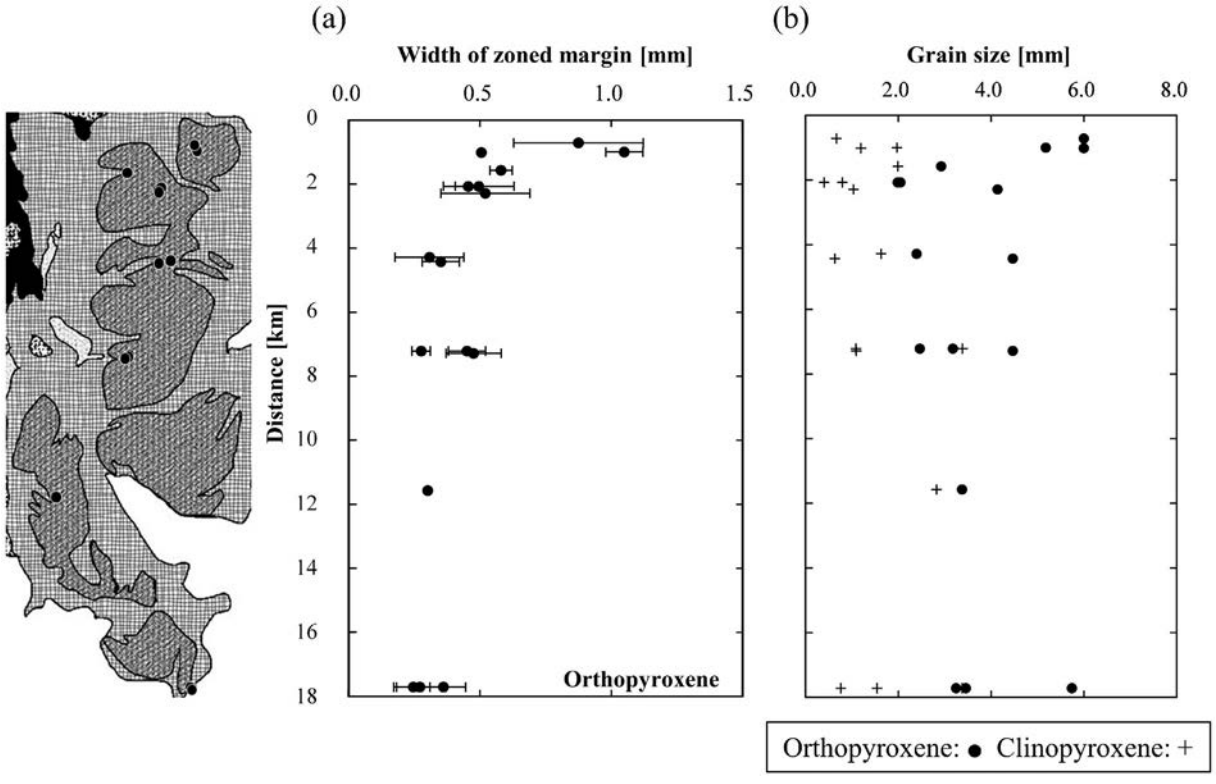

Fig. 13. (a) Mean widths of zoned and lamella-free margins of orthopyroxenes and (b) grain sizes of the pyroxenes analyzed for the line profiles shown in Figs. 4–9, plotted against the distance measured from the northern end of the Lanzo Massif along a N—S line by projecting along the E–W direction. The widths shown in (a) are defined by the zones where Ca contents start to decrease towards the rims of the orthopyroxene, and which correspond roughly to a scarcity or absence of exsolution lamellae. The mean values of grain size based on the entire lengths of the line analyses for each sample. The error bars are ±1σ.

(pressure and temperature trajectory) taken by the Lanzo complex have until now been sketchy. The remarkable zoning patterns of Al and Cr require the maintenance of high temperatures to promote the diffusion of Al and Cr on a grain scale of ~5 mm, which suggests a decompression path with suppressed cooling. Because of the much slower diffusion of Al than Ca in pyroxene (Chakraborty, 2010; Cherniak and Dimanov, 2010; Ganguly et al., 2007; Smith and Barron, 1991), the trapezoidal Ca zoning and bell-shaped Al zoning patterns indicate that the cooling-induced exsolution in the pyroxenes should have started after the Al zoning was fully developed. The exsolution of mutual pyroxene phases inhibits the net diffusion of Ca from the cores to the grain boundaries unless the cooling is very slow.

The most plausible exhumation history is therefore one of nearly adiabatic decompression through the plagioclase peridotite field at an early stage, followed by decompression accompanied by effective cooling after reaching a shallow-enough depth. We have constructed a diffusion model to reproduce the development of the Al and Ca zoning (Ozawa, 1997, 2004) and some results are presented in Appendix B. We tested decompression along various pressure–temperature paths under constant rates of ascent, and we found that the observed differences in the zoning patterns of Al and Ca are reproduced only if the decompression is nearly adiabatic at high temperatures (see Appendix B and Fig. A2). The remarkable development of Al zoning with suppressed Ca zoning in the pyroxenes can be attributed to the strongly negative Al isopleths and weakly positive Ca isopleths of pyroxenes in the plagioclase peridotite facies (Gasparik, 1984, 2003; Fig. A2a).

The pattern of Ca zoning in olivine, with a decrease in Ca contents towards the contacts with pyroxenes, also indicates a monotonous cooling history, but due to the higher diffusivity of Ca in olivine than in pyroxenes, the zoning in the olivine was frozen at temperatures that were lower than those inferred from the Ca zoning in the pyroxenes. This will become clearer below after we describe the results of applying a geothermometer to the olivine compositions.

The decompression accompanied by cooling and deformation undergone by the Lanzo Massif is the essential basis for reconstructing the original structure of the massif before its exhumation. In order to accomplish this task, we need to assess whether the compositions of the constituent minerals reflect the pressures and temperatures under which the massif resided for a certain period of time, or whether those compositions were frozen in place due to the kinetic hindrance of relevant reactions during cooling. The compositions that most unequivocally represent a residence condition are the Ca contents of the pyroxene cores. This is because the patterns of Ca zoning are characterized by a flat-top trapezoidal pattern in the orthopyroxenes and a bottom-flat pattern for the clinopyroxenes, which can be attributed to the process of exsolution in the pyroxenes that enabled the flat-core composition representing the condition of prolonged residence of the rocks in the mantle to be frozen in place. On the other hand, the rim compositions of the pyroxenes were kinetically frozen at a certain temperature during the period of continuous cooling. This temperature can be called the "closure temperature" sensu *lato*, which can be defined as "the calculated temperature that stops decreasing due to the net cessation of the relevant reactions during the continuous cooling". This is a looser definition of "closure temperature" sensu stricto as given by Dodson (1973).

8.2. Methods of geothermometry

The geothermometers we used were (1) the Ca-in-orthopyroxene geothermometer of Lindsley (1983), (2) the Ca-in-orthopyroxene geothermometer of Brey and Köhler (1990), (3) the two-pyroxene geothermometer of Brey and Köhler (1990), (4) the two-pyroxene geothermometer of Taylor (1998), (5) the two-pyroxene geothermometer of Wells (1977), and (6) the Ca-in-olivine geothermobarometer calibrated on the basis of the experimental results of Köhler and Brey (1990) (see Appendix A). Nimis and Grütter (2010) evaluated geothermometers extensively, and they showed that the two-pyroxene thermometer (4), which they considered the best, gave results consistent with those obtained with (2) and (3) for Na-poor clinopyroxene for temperatures in the range of 1000–1400 °C. If there is strong zoning, a geothermometer based on the chemical compositions of two or more minerals has the notable problem of specifying which mineral pair was in equilibrium, which in practice is difficult. The two-pyroxene geothermometers (3) to (5) require orthopyroxene and clinopyroxene and have this inherent problem. In the case of our samples, the geothermometers (3) to (5) have another difficulty, which is the presence of thick exsolution lamellae in the clinopyroxenes and the patchy topotaxic orthopyroxene in the clinopyroxene cores, which complicates attempts to estimate the bulk core composition. Our principle strategy in the geothermometry was to use the components of a single phase coexisting with another phase, fixing the composition of the former at a given temperature and pressure, and thus we used (1) and (2) for the lherzolite system. In the application of these thermometers, pressure was assumed to be 1 GPa. We tested lower pressures (0.5 and 0.1 GPa), and these gave lower temperatures up to 30 °C/GPa. The Al contents of the pyroxenes and the values of Ca/Na in the plagioclases can be used as geothermobarometers (Fumagalli et al., 2017; Gasparik, 2003), but more accurate pressures cannot be estimated than those reported by (Fumagalli et al., 2017) because of the strong Ca—Na zoning and slow Ca—Na interdiffusion in plagioclase, and because of the notable Cr-dependency of Al solubility in the pyroxenes.

In order to remove the effects of grain size dependence, we were able to confirm that the grain sizes of the pyroxenes we analyzed do not show any systematic spatial variation in the Lanzo Massif (Fig. 13b). We also tested the grain size dependence of mean core compositions and found that grains >3 mm in size gave essentially the same mean compositions (Fig. S10). We used sample mean and standard errors by taking a weighted mean composition for each sample for grains of >3 mm in size, to examine spatial variations in the calculated temperatures in the Lanzo Massif (see the next section).

8.3. Geothermometry of the Lanzo Massif

Temperatures calculated with geothermometers (1) to (6) are listed in Table 3 and those calculated with (1), (3), and (6) are plotted on Fig. 14. The temperatures calculated with the Ca-in-orthopyroxene geothermometer (1) for the cores and rims lie in the ranges of 1120–1240 °C and 940–1180 °C, respectively (Fig. 14a). The temperatures for the cores are systematically higher than those for the rims, and both decrease from south to north. The differences in temperature between the cores and rims increase from south to north. The same results were obtained with geothermometer (2) (Fig. S12b). The temperatures calculated with geothermometer (3) for the cores and rims of two pyroxenes lie in the ranges of 850–1150 °C and 800–1000 °C, respectively (Fig. 14b). The temperatures for the cores are systematically higher than those for the rims, and both decrease from south to north. The differences in temperature between the cores and rims are much smaller than those given by the Ca-in-orthopyroxene thermometers, and they do not show any spatial variations (cf. Fig. 14a and b). The same results were obtained with the two-pyroxene geothermometers (4) and (5) (Fig. S12d and e). The temperatures calculated with geothermobarometer (6) for the cores and rims of olivine lie in the ranges of 600–1000 °C and 400–900 °C, respectively (Fig. 14c). The temperatures for the cores of olivine are systematically higher than those for the rims, and both decrease from south to north, as was the case for the Ca-in-orthopyroxene and two-pyroxene geothermometers. The temperatures based on Ca-in-olivine (Fig. 14c) are systematically lower than those based on Ca-in-orthopyroxene (Fig. 14a). The temperatures based on the two-pyroxene thermometers (Fig. 14b) are systematically lower than those calculated with the Ca-in-orthopyroxene thermometer (Fig. 14a). The Ca-in-orthopyroxene geothermometer yields

systematically higher temperatures than the two-pyroxene geothermometers, irrespective of which geothermometers were used, some of which have been shown to be reliable by Nimis and Grütter (2010). This result can be attributed to the two pyroxenes in the Lanzo Massif not providing proper core–core equilibrium pairs, the reasons for which are discussed below.

As mentioned above, the profiles of Ca in the orthopyroxenes show a plateau in each core region, after taking averages over distances of more than a few hundred μm to include the exsolution lamellae of clinopyroxene. This records a high temperature condition, where the Lanzo Massif resided for a long time. On the other hand, there are several reasons why it is difficult to obtain high-temperature records for the cores of clinopyroxenes. First, the clinopyroxenes are always approximately half the size of orthopyroxenes, though elemental diffusion is slower in the clinopyroxene. Second, the clinopyroxene cores contain patches of orthopyroxene as large as a few hundred μm, prohibiting the proper estimation of core compositions, and suggesting a complex history recorded in the core regions. Third, clinopyroxene grains exhibit extensive grain boundary migration, which intruded even into the primary core regions. In fact, the temperatures obtained by two-pyroxene thermometry are systematically lower than those obtained by the Ca-in-orthopyroxene geothermometer, and the temperature differences between the cores and rims are small or almost insignificant. We conclude, therefore, that the calculated temperature variations from the cores of orthopyroxene, using thermometers (1) or (2), represent most faithfully the thermal structure of the massif at the place where it resided in the mantle for a long period of time, probably close to the lithosphere–asthenosphere boundary (LAB) zone before exhumation of the massif.

The pressure constraints for this prolonged stage of residence at temperatures of 1100–1200 °C come from the large aluminous spinel grains (up to 5 mm) that are rimmed with plagioclase in the peridotites and pyroxenites (Boudier, 1978) and also from the clinopyroxenes of both lithologies,that show weak negative Eu anomalies and HREE abundances that are too high to have been in equilibrium with garnet even after correction for plagioclase crystallization (Bodinier et al., 1991; Guarnieri et al., 2012; Takazawa et al., 1996). These two observations imply the presence of aluminous spinel and the absence of garnet in both the peridotites and pyroxenites before plagioclase crystallized through the consumption of spinel. This situation was realized by the residence of the Lanzo Massif in the Seiland subfacies during the high temperature stage. This means that the depth must have been shallower than ~40 km, equivalent to ~1.2 GPa. Boudier and Nicolas (1972) and Boudier (1978) postulated, without evidence, that the Lanzo Massif had ascended from a depth of at least 100 km. Piccardo et al. (2007) argued that the Lanzo Massif had come from the depth of the garnet peridotite facies on the basis of intergrowths of orthopyroxene and spinel found in less fertile peridotites. However, such microstructures have been reported from abyssal peridotites formed at shallower levels through a process involving decompression melting and a series of reactions with the interstitial melt (Suhr et al., 2008). Continuous decompression from the garnet stability field is not consistent with the presence of the patchy topotaxic orthopyroxene in large clinopyroxene grains (Fig. 7b, d), and instead a period of cooling is indicated, which was followed by a long period at a high temperature in the spinel stability field before the decompression of the Lanzo Massif.

The proximity of the Lanzo Massif to the LAB zone is suggested by the high temperature of this stage (1100–1200 °C) and the pervasive or focused percolation of melts that produced the diverse lithologies of the Lanzo Massif (e.g., Piccardo et al., 2007). A nearly adiabatic decompression path from a depth of ~40 km at the temperature obtained from the cores of orthopyroxenes (1200 °C for the southern body) barely crosses the dry solidus of a fertile peridotite at ~0.7 GPa (Fig. 15). This adiabatic decompression could have provided a suitable thermal state for reactive melt transportation in the southern body, which might be related to the formation of feldspathic lenses and

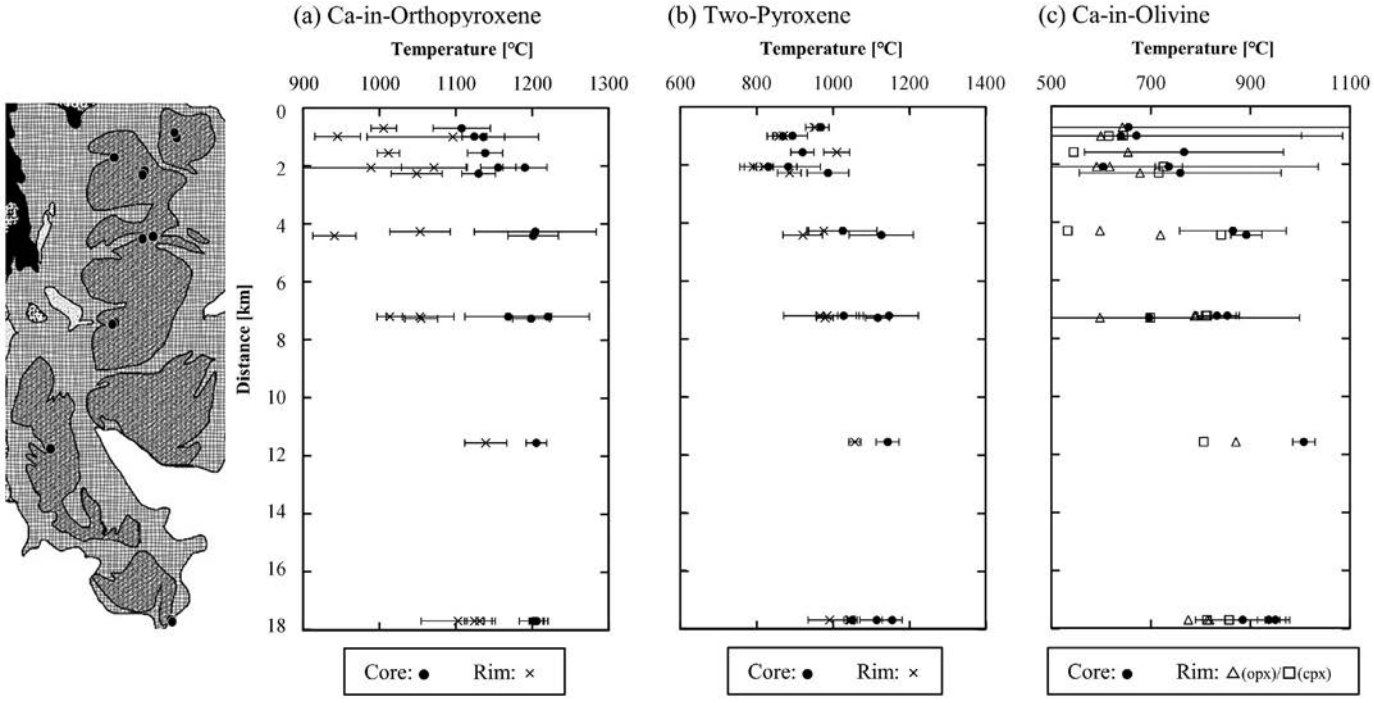

Fig. 14. Spatial variations in the temperatures in the Lanzo Massif calculated with the Ca-in-orthopyroxene geothermometer of Lindsley (1983) (a), the two-pyroxene geothermometer of Brey and Köhler (1990) (b), and the Ca-in-olivine geothermobarometer calibrated on the basis of the experimental results of Köhler and Brey (1990) (c). The calculated temperatures are plotted against the distance measured from the northern end of the massif along a N—S line by projecting along the E–W direction. The solid circles indicate calculated temperatures for the cores, crosses indicate temperatures for pyroxene rims, open triangles for olivine rims in contact with orthopyroxene, and open squares for olivine rims in contact with clinopyroxene. See Appendix for details of the recalibration of the Ca-in-olivine thermobarometry.

Table 3
Calculated temperatures (°C) for the examined plagioclase peridotites.

Unit	Sample	Geothermometers																
		Ca-in-Orthopyroxene (Lindsley, 1983)						Ca-in-Orthopyroxene (Brey and Köhler, 1990)						Ca-in-Olivine based on (Köhler and Brey, 1990)				
		Core			Rim			Core			Rim			Core			Rim	
																	Ropx	Rcpx
North	100807	1108	±	38	1005	±	17	1140	±	32	991	±	17	655	±	483	643	483
	100806A	1124	±	16	945	±	30	1115	±	18	927	±	30	671	±	331	641	645
	100805	1136	±	28	1096	±	113	1122	±	43	1061	±	110	640	±	445	600	616
Shear zone	100801A	1138	±	23	1011	±	15	1190	±	35	1003	±	13	767	±	200	654	545
	100701A	1130	±	22	1048	±	33	1122	±	29	1029	±	35	759	±	203	678	716
	100703	1156	±	23	988	±	127	1154	±	24	982	±	120	604	±	432	618	429
	100706B	1191	±	29	1071	±	43	1124	±	20	1057	±	47	736	±	27	591	725
Central	100405	1204	±	80	1053	±	40	1166	±	71	1056	±	46	865	±	107	598	533
	100408	1201	±	33	940	±	28	1176	±	30	918	±	40	892	±	31	720	841
	100401B	1199	±	24	1054	±	22	1152	±	24	1070	±	30	697	±	302	598	699
	100315	1169	±	57	1053	±	45	1047	±	43	1044	±	46	854	±	24	788	810
	100314C	1221	±	54	1013	±	17	1209	±	59	1018	±	17	833	±	38	791	813
South	100509D	1206	±	14	1139	±	28	1193	±	14	1129	±	29	1007	±	22	871	806
	1005pz1A	1202	±	19	1131	±	16	1207	±	16	1163	±	17	950	±	21	818	858
	062505A	1206	±	10	1103	±	49	1207	±	10	1097	±	49	937	±	22	775	813
	062504	1206	±	9	1124	±	13	1202	±	9	1119	±	14	885	±	94	813	857

Unit	Sample	Geothermometers																
		Two-Pyroxenes (Brey and Köhler, 1990)						Two-Pyroxenes (Taylor, 1998)						Two-Pyroxenes (Wells, 1977)				
		Core			Rim			Core			Rim			Core			Rim		
North	100807	969	±	21	952	±	23	939	±	21	913	±	19	967	±	17	958	±	14
	100806A	895	±	39	871	±	27	869	±	42	830	±	23	917	±	27	902	±	17
	100805	869	±	27	858	±	30	840	±	24	833	±	24	897	±	16	899	±	17
Shear zone	100801A	921	±	30	1010	±	34	869	±	29	949	±	40	914	±	18	997	±	31
	100701A	987	±	55	886	±	31	950	±	49	843	±	26	975	±	35	910	±	18
	100703	884	±	84	791	±	23	888	±	53	753	±	15	934	±	36	848	±	10
	100706B	831	±	75	818	±	26	848	±	72	791	±	21	903	±	49	870	±	13
Central	100405	1026	±	89	976	±	44	1032	±	78	934	±	35	1065	±	74	987	±	26
	100408	1127	±	84	922	±	52	1094	±	64	863	±	46	1115	±	65	933	±	32
	100401B	1118	±	31	979	±	22	1092	±	33	936	±	33	1102	±	33	979	±	26
	100315	1147	±	78	985	±	29	1080	±	75	954	±	18	1117	±	76	998	±	14
	100314C	1028	±	52	966	±	95	1013	±	48	907	±	77	1013	±	53	978	±	58
South	100509D	1144	±	30	1058	±	15	1114	±	30	1022	±	11	1122	±	30	1051	±	9
	1005pz1A	1156	±	26	1047	±	9	1114	±	26	1015	±	6	1126	±	28	1046	±	5
	062505A	1050	±	13	992	±	57	1019	±	12	956	±	40	1035	±	11	997	±	32
	062504	1115	±	44	1043	±	14	1071	±	19	1003	±	11	1085	±	18	1035	±	9

Abbreviations; Ropx: olivine rim in contact with orthopyroxene, Rcpx: olivine rim in contact with clinopyroxene.

veinlets (Boudier, 1978; Boudier and Nicolas, 1972) and the "indigenous dunite" with harzburgite margins (Boudier, 1978; Boudier and Nicolas, 1972; Piccardo et al., 2007; Sanfilippo et al., 2014, 2017, 2019). If water had been present, which is suggested by the occurrence of amphibole in the northern shear zone (Kaczmarek and Müntener, 2008; Kaczmarek and Tommasi, 2011), partial melting and reactive melt percolation would be expected even in the northern part of the Lanzo Massif during decompression (Fig. 15).

It is likely that the thermal gradient estimated from the variations in the calculated temperatures from pyroxene cores and the distances among the sample localities in the massif may record the thermal structure of the lithosphere close to the LAB zone, with the southern body closer to or within the LAB. In contrast, the temperatures calculated from the rims of orthopyroxenes and the cores and rims of olivine represent temperatures during the cooling from the lithospheric conditions estimated above, and they can be regarded as closure temperatures sensu *lato*, as mentioned before. Therefore, the decrease in closure temperature from south to north in the Lanzo Massif indicates a decrease in cooling rate from south to north at approximately the time when the closure temperatures were attained. The increases in the mean widths of the lamella-free and Ca-decreasing marginal zone of orthopyroxene grains from south to north (Fig. 13a) and the decreases in Ca in the marginal zones also suggest that the cooling rate in the southern body was higher than in the northern body at temperatures before the onset of the nucleation and growth of exsolution lamellae. This possibility is examined in the next section.

8.4. Exhumation history of the Lanzo Massif

Fig. 15 illustrates a model for the temporal change of the thermal structure of the Lanzo Massif, as inferred from the data presented above. The Lanzo Massif originally resided near a LAB zone at near solidus conditions, and maintained its thermal structure on a scale of ~20 km. The southern body may represent either cooled asthenosphere that became part of the lithosphere (lithospheric thickening) (Bodinier et al., 1991) or lithospheric mantle close to the LAB (Müntener et al., 2005; Piccardo et al., 2007; Sanfilippo et al., 2014, 2017, 2019) that interacted with melt derived from the underlying asthenosphere in the LAB zone (the lithospheric thinning or asthenospherization of Müntener et al., 2005). The original thermal structure is recorded in the cores of orthopyroxene grains as bulk Ca concentrations. The northern body may represent cooler lithospheric mantle that ascended from the spinel peridotite field. A cooler environment and shallower original depth are suggested by the incomplete breakdown reaction of two

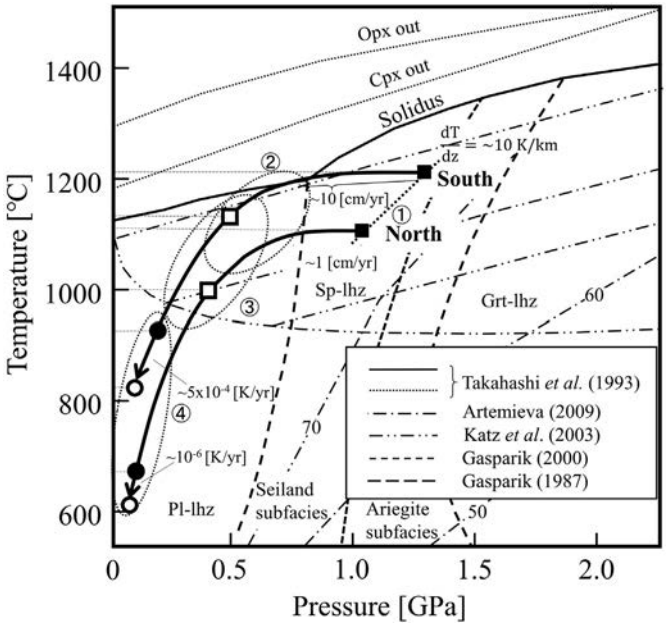

Fig. 15. Inferred pressure and temperature (P–T) trajectories taken by the northern and southern bodies of the Lanzo Massif, with timescales for decompression and cooling indicated on the P–T paths. In this model, the entire Lanzo Massif originally stayed at the different temperatures and pressures shown by solid squares for the southern and northern bodies. The absolute pressure conditions are unknown, but the relative depths were estimated from the distance across the northern and southern bodies, which gives a thermal gradient of ~10 K/km. The first stage of decompression was nearly isothermal with a limited decrease in temperature and at a rate of 1 cm/year for the northern body and 10 cm/year for the southern body, during which the Al and Cr zoning was developed in the pyroxenes. This first stage was followed by cooling stages (2), (3), and (4). The Lanzo Massif (in both the northern and southern bodies) underwent significant deformation during the later isothermal stage as well as during the earlier cooling stage (2), as suggested by several microstructures that constrain the timing of deformation during the P–T changes. During cooling stage (3), the exsolution lamellae in pyroxenes formed, and the compositions of pyroxene rims and olivine cores and rims were sequentially frozen depending on the respective reaction kinetics and cooling rates, as shown by open squares for the pyroxene rims, solid circles for the olivine cores, and open squares for the olivine rims. The closure temperatures show a systematic decrease from south to north, indicating that the cooling rate decreased in this direction. The cooling rate for the southern body is estimated to have been 5×10^{-4} K/year at 800 °C and that for the northern body 10^{-6} K/year at 650 °C. The fine solid, thick solid, and dotted lines are after Takahashi et al., 1993 and they show respectively the dry lherzolite (KLB-1) solidus and the stability limits of clinopyroxene and orthopyroxene determined in melting experiments. The dashed curves are the peridotite facies boundaries in the CFMAS system (Pl-lhz, plagioclase lherzolite facies; Sp-lhz, spinel lherzolite facies; Grt-lhz, garnet lherzolite facies; Gasparik, 1987). The double-dotted and dashed curves are the compiled dry solidus after Hirschmann (2000) and the wet solidus and water-present solidi after Katz et al. (2003), respectively. The dot–dashed curves are model geotherms for the subcontinental lithosphere after Artemieva (2009) for surface heat flows of 50, 60, and 70 mW/m^2.

pyroxenes and spinel to olivine and plagioclase, which is suggested by the occurrence of the 5–10 cm thick layers of "ariegite" only in the central and northern bodies (Bodinier, 1988; Boudier, 1978) and by the intimate spatial association of large spinel grains and plagioclase in the plagioclase lherzolites in the northern part of the Lanzo Massif.

The temperatures and pressures as the mantle started to exhume and cool are recorded by the patterns of zoning in the pyroxenes. The absence of flat Al and Cr core regions requires enhanced Al and Cr diffusion and the suppressed modification of the core Ca contents, which could only have been achieved by nearly adiabatic decompression through the plagioclase peridotite facies, as discussed above (see Appendix B and Fig. A2). During this stage of decompression, the thermal gradient of the lithosphere was maintained. Possible ranges of the timescale of this stage of nearly adiabatic decompression can be estimated from the half size of large orthopyroxene grains (1.5 mm) and the diffusion coefficient of Al in orthopyroxene, as constrained by Smith and Barron (1991), based on the zoning of Al in natural samples and an activation energy of 400 kJ/mol. The estimates are ~0.2 myr at 1200 °C for the southern body and ~2 myr at 1100 °C for the northern body. These timescales translate into decompression rates of ~1 cm/year for the northern body and ~10 cm/year for the southern body. The minimum estimates for the timescales are much shorter than the time gap between the Alpine metamorphism, dated at 55 Ma by Rubatto et al. (2008), and the 158–163 Ma gabbro dikes that were intruded into the peridotite host at low pressures (Kaczmarek et al., 2008). At some moment, a depth-dependent differential motion of the lithosphere started cooling that proceeded in different ways depending on the depth (Fig. 15). The concentric zoning of Ca and the exsolution lamellae in pyroxenes formed during this stage. A rotation of the Lanzo Massif started to cause depth-dependent decompression and differential cooling, with more rapid ascent and a higher cooling rate in the deeper southern body than in the shallower northern body (Fig. 15).

Closure temperatures frozen during the cooling that accompanied the exhumation were recorded as Ca contents in the rims of orthopyroxenes and clinopyroxenes and as Ca contents in the cores and rims of olivine, and all these closure temperatures decrease from north to south. This spatial trend indicates rapid cooling in the high-temperature deep zone (represented by the southern body) and slower cooling in the low-temperature shallow zone (represented by the northern body) (Fig. 15). Cooling rates in the final stage, when the patterns of Ca zoning in olivine were frozen, were estimated by reproducing the zoning (Fig. A3) with a diffusion model assuming a constant cooling rate (see Appendix C and Fig. A3). The optimized cooling rates are 10^{-6} K/year at ~650 °C for the northern body and 5×10^{-4} K/year at ~800 °C for the southern body (Fig. 15). This difference in cooling rate may be explained by an early started, slow, and protracted ascent of the northern body and a late but quick exhumation of the southern body.

The restored decompression history of the Lanzo complex, as recorded by the zoning of the olivine, stops at a temperature of 650 °C, which is the minimum temperature registered by the Ca contents of the olivine rims in the northern body. The chemical compositions and patterns of zoning in the olivines and pyroxenes could not change at all below this temperature, unless the massif resided at a temperature below 650 °C for a long time. The Lanzo Massif is known to have undergone the Alpine high-pressure metamorphism before its exhumation (Debret et al., 2013; Kienast and Pognante, 1988; Lagabrielle et al., 1989; Pelletier and Müntener, 2006). The peak metamorphic temperature has been estimated to be 620 °C (Pelletier and Müntener, 2006). The diffusion coefficient of Ca in olivine (Coogan et al., 2005) and the observed Ca zoning over a distance of ~1 mm in the olivines of the northern body (Fig. 10e) allow us to calculate that a period of ~100 myr would have been required to modify the Ca zoning. This amount of time is one order of magnitude greater than the timescale of the metamorphism (~8 myr) (Rubatto et al., 2008). We conclude, therefore, that the Alpine metamorphism did not modify the compositions of the primary minerals in the Lanzo Massif.

Lagabrielle et al. (1989) found a metasedimentary cover of ophicarbonates, Mn-rich metaquartzites, and metabasites in a serpentinite envelope of the Lanzo Massif, which underwent the Alpine metamorphism (Pelletier and Müntener, 2006). Debret et al. (2013) found that lizardite had been replaced by antigorite in peridotites of the Lanzo Massif during a prograde stage of the Alpine metamorphism. These observations clearly show oceanization of the Lanzo Massif and its serpentinite envelope (Debret et al., 2013), during which sea-floor metamorphism of the Lanzo Massif took place by the introduction of fluids. This event can be understood as an extension of the cooling of the Lanzo Massif, which otherwise left no record below the temperature of 650 °C, with this temperature constrained by the Ca zoning of the olivine (Fig. 14).

8.5. Deformation in the framework of the pressure–temperature path

The Lanzo Massif could have undergone deformation from near the lherzolite solidus conditions down to the conditions of Ti-pargasitic amphibole stability, at least in the northern shear zone (Boudier, 1978; Kaczmarek and Tommasi, 2011). Understanding this deformation, which may have separated and individualized the three bodies (northern, central, and southern) at a particular stage of exhumation of the massif, is important if we are to reconstruct and understand the evolution of the tectonic framework of the Ligurian–Piedmontese basin and the Adriatic margin. In order to clarify the timing of deformation during the exhumation, which would have occurred along the pressure–temperature path inferred above, we have to establish unequivocally the relationships between deformation-related microstructures and the temperature and pressure records. This can be achieved by examining the relationships between the microstructures and the compositional zoning of the minerals, and this has already been done for the spinel and plagioclase. Here, we will now examine further the relationships for the pyroxenes.

The grain boundary indentations into the Al-rich cores of clinopyroxene that contain patchy topotaxic orthopyroxene, and the thinner zones of Al depletion along the indentations (Fig. 7b and d), can be attributed to grain boundary migration after the development of the Al zoning and the nucleation and growth of the patchy orthopyroxene. The grain boundary migration must have taken place almost simultaneously with the formation of the zones with sharply decreasing Al contents near the rims. These rims mark the final stages in the development of Al zoning shortly before the freezing of the Al zoning profile, which means, therefore, that the cooling must have started during the grain boundary migration. The patchy orthopyroxene formed probably as a result of long residence at a high temperature close to the solidus or even above the solidus before the onset of cooling. Because the patchy orthopyroxene is in a topotaxic relationship with the host clinopyroxene, we speculate that it grew from thinner exsolution lamellae of orthopyroxene that formed during an earlier stage of cooling in the subcontinental lithospheric mantle, possibly in the spinel peridotite field, as advocated by Pognante et al. (1985), Piccardo et al. (2007), and Kaczmarek and Müntener (2008).

The pattern of Ca zoning in orthopyroxene, where local high-Ca bands occur along tilt boundaries in a Ca depletion zone without disturbance of the Al zoning, suggests that the orthopyroxene grains underwent deformation before or during a time when Ca diffusion was effective on a scale of a few hundred microns but after the Al zoning was almost fully developed, implying that the deformation of orthopyroxene took place at the start of cooling following the nearly adiabatic decompression. This stage of deformation in the orthopyroxene was penecontemporaneous with the grain boundary migration of the clinopyroxene, which also followed the development of Al zoning, but at a higher temperature, creating the sharp changes in composition in the outermost rims on a scale of ~100 μm. The stage of deformation indicated by the pyroxenes is consistent with that indicated by the spinel and plagioclase, as discussed above. The deformation of the pyroxenes, spinel, and plagioclase also implies deformation of the olivine, which is the major constituent of the peridotites. We conclude, therefore, that the Lanzo Massif underwent deformation at a time when the nearly isothermal decompression changed to effective cooling, probably accompanied by further decompression.

The timing of the start of the exhumation of the mantle, accompanied by deformation, is recorded in the zoning patterns of the pyroxenes, spinel, and plagioclase, the off-centered Al maxima in the clinopyroxene with patchy orthopyroxene that indicate extensive grain boundary migration in clinopyroxene, the subgrain formation in orthopyroxene with the development of exsolution lamellae, the deformation induced Al—Cr zoning in spinel, and the preferred growth of plagioclase in the direction of elongation, which defines the lineation.

The zoning of Al and Cr in the pyroxenes developed mostly during nearly isothermal decompression after the Lanzo Massif had ascended into the stability field of plagioclase (Borghini et al., 2010), which caused the decomposition of spinel, the crystallization of plagioclase, and the development of Al—Cr and Ca—Na zoning in these minerals. The deformation therefore promoted the diffusion creep in the spinel and the anisotropic growth of plagioclase during this period of nearly isothermal decompression (Fig. 15). The grain boundary migration observed in the clinopyroxene and the tilt boundary formation in the orthopyroxene must have taken place at a later stage of development of the Al and Cr zoning in the pyroxenes. We infer, therefore, that the deformation took place mainly during the final stage of the isothermal decompression, and that it continued during the early stage of cooling with limited decompression.

During the early stage of decompression, the deformation of the lithosphere above the LAB zone was probably uniform, but a differential depth-dependent motion of the lithosphere inevitably developed, and this non-uniform deformation was then responsible for the depth-dependent cooling history of the Lanzo Massif (Fig. 15).

Kaczmarek and Müntener (2010) argued that the northern shear zone underwent modification by melts derived from the asthenosphere related to deformation during exhumation of the massif. Higgie and Tommasi (2014) also argued that the deformation in the northern shear zone took place in the presence of a partial melt. Our temperature estimates for the cores of orthopyroxenes in the northern shear zone using the Ca-in-orthopyroxene geothermometer are notably scattered. Jollands and Müntener (2019) determined the bulk compositions of orthopyroxene cores in samples from the northern shear zone using laser ablation inductively coupled plasma mass spectrometry, and they obtained consistent temperatures of 1150–1200 °C using the modified Ca-in-orthopyroxene geothermometer. These temperatures are comparable to our estimates for sample 100706B (Table 1), which came from their study area. The large scatter in our temperatures suggests a local thermal anomaly and a high thermal gradient in this region.

8.6. Implications for the geothermal gradient near the LAB zone

We found above that the original temperatures before decompression in the spinel peridotite facies decrease from south to north in the Lanzo Massif, suggesting preservation of the original thermal gradient in the massif, although we are not sure if the thermal gradient was vertically developed or horizontally developed because of the absence of reliable geobarometry. In order to estimate the thermal gradient, we need to estimate the original distances in the massif. We assume that the depth can be measured perpendicular to the foliation, giving a distance of ~10 km from the southern outcrops to the northern outcrops. We can then calculate the geothermal gradient as ~10 K per kilometer, presuming there was no thinning during exhumation. Though this value may have a large uncertainty because of the shortening and/or rearrangement of the northern, central, and southern bodies (Boudier and Nicolas, 1977), this thermal gradient is significantly larger than its common value near the thermally steady-state LAB zone, which is estimated to be ca. 3–4 K per kilometer (McKenzie et al., 2005). If the thermal structure represents the geotherm, such a steep geothermal gradient implies the existence of some thermal perturbation around the LAB zone, which might be attributed to the involvement of the hotter asthenospheric mantle.

9. Conclusions

Grain-scale compositional heterogeneities in the constituent minerals of the plagioclase peridotites in the Lanzo Massif of northern Italy provide us with a better understanding of its decompression history and its initial thermal structure. The compositional zoning in the orthopyroxene, clinopyroxene, olivine, spinel, and plagioclase suggests continuous decompression and cooling,

accompanied by deformation, throughout the exhumation of the massif. The systematic differences in the patterns of Al, Cr, and Ca zoning in the pyroxenes indicate that the early stage of decompression was nearly isothermal, and that this was followed by intensive cooling with relatively minor decompression. Careful examination of the relationships between deformational microstructures, the compositional zoning of minerals, and exsolution phenomena, leads to the conclusion that the deformation took place mainly during the earlier stages of effective cooling.

Variations in the mean mineral compositions on the scale of the massif suggest variations in the cooling history of the massif. The systematic decreases in all calculated temperatures from the southern body towards the northern body are clarified. All the variations and differences in closure temperatures recorded by the rims of pyroxenes and the rims and cores of olivine indicate that the northern body cooled at a slower rate than the southern body at temperatures in the range of 1000–600 °C. The initial temperatures, recorded by the minerals before the start of exhumation, decrease systematically from south to north in the massif by ~60 K, and this may represent the geotherm near the LAB zone with a geothermal gradient of ~10 K per kilometer. If this represents the thermal gradient of the ancient LAB zone, its value is significantly steeper than in deep lithosphere at a steady state, and it may therefore represent a thermal perturbation caused by the underlying and hotter asthenospheric mantle.

Supplementary data to this article can be found online at https://doi.org/10.1016/j.lithos.2020.105661.

Declaration of Competing Interest

This manuscript has not been published and is not under consideration for publication in any other journals, and we have no conflicts of interest associated with this publication.

Acknowledgments

The authors thank H. Yoshida for valuable assistance with the electron microprobe analyses, T. Iizuka and S. Wallis for daily discussions, C. Garrido for discussions and help with the field work in the Lanzo Massif, and A. Zanetti and other members of the organizing committee of the 3rd EMAW for giving us the opportunity to write this manuscript. The authors thank three anonymous reviewers for their thorough and critical reviews, which significantly improved the manuscript. Comments and suggestions from the guest editor C. Bonadiman were greatly appreciated. This study was supported by Japan Society for the Promotion of Science (JSPS) KAKENHI grants: Grant Numbers 21340158, 17H02982, and 20H02003.

Appendix A

In this appendix we describe the calibration of the Ca-in-olivine geothermobarometer on the basis of experiments in the peridotite system performed by Köhler and Brey (1990). Köhler and Brey (1990) calibrated the geothermobarometer on the basis of the Ca exchange reaction between olivine and clinopyroxene, which is often incorrectly called the Ca-in-olivine geothermobarometer. In order to apply the experimental results to natural rocks with minerals that display significant zoning, a single mineral geothermobarometer is more appropriate than that based on exchange reactions, because this reduces the uncertainties created by attempting to pair minerals that are heterogeneous. This was the motivation behind the recalibration of the Ca-in-olivine geothermobarometer.

In the calibration, the pressure dependencies of the Ca exchange reaction among olivine, orthopyroxene, and clinopyroxene are fixed according to Sack and Ghiorso (1994) for pyroxenes and Hirschmann (1991) for olivine, because the Ca content in olivine is more sensitive to changes in pressure. On the basis of this, we optimized one parameter by reproducing the experimental results of Köhler and Brey (1990) (Fig. A1). The obtained calibration is as follows:

$$T = \frac{8573 + 517 \times P}{13.5 - \ln(C_{Ca})}$$

where T is the temperature in Kelvin, P is the pressure in GPa, and C_{Ca} is the concentration of Ca in olivine in ppm.

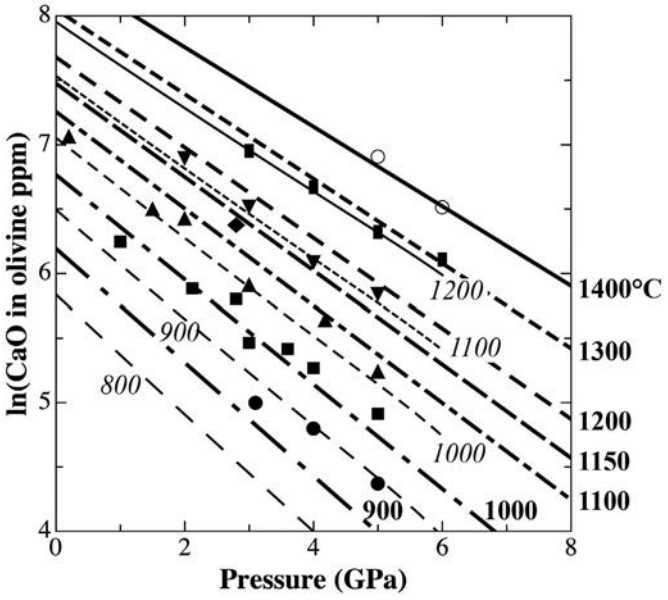

Fig. A1. Experimentally determined CaO contents of olivine coexisting with orthopyroxene and clinopyroxene after Köhler and Brey (1990), shown by symbols representing temperatures of 900 °C (solid circles), 1000 °C (solid squares), 1100 °C (solid triangles), 1150 °C (solid diamonds), 1200 °C (solid inverted triangles), 1300 °C (solid rectangles), and 1400 °C (open circles). The thick isopleths represent a one-parameter calibration to reproduce the experimental results with pressure dependence that is consistent with the thermodynamic model for pyroxenes after Sack and Ghiorso (1994) and that for olivine after Hirschmann (1991), shown as thin isopleths with the same line pattern for equivalent temperatures.

Appendix B

In this appendix we describe how we constrained the pressure and temperature trajectory taken by the Lanzo complex during its exhumation. This was done by reproducing the contrasting profiles for Al and Ca zoning in the orthopyroxenes (Fig. 5), which are characterized by remarkable changes in composition from the cores to the rims without any flat region for Al, and with a flat core and marginal depletions for Ca. The model adopted is basically the same as that developed by Ozawa (1997, 2004), and it assumes rapid reaction and transportation in the matrix of a large spherical orthopyroxene grain and diffusive transportation within the grain. The equilibrium relationship in the matrix is according to Gasparik (2000) in the CaO–MgO–Al_2O_3–SiO_2 system (Fig. A2a). The diffusion coefficient of Al in orthopyroxene is constrained by using a relationship between the activation energy and the pre-exponential term obtained by reproducing the Al zoning in orthopyroxene included in garnet in the ultramafic diatremes on the Colorado Plateau (Smith and Barron, 1991). The activation energy is constrained to be larger than 400 kJ/mol, which is assumed to fix the Arrhenius relationship. The value of the diffusion coefficient of Ca in orthopyroxene is not available, and we assumed therefore that the diffusivity is one order of

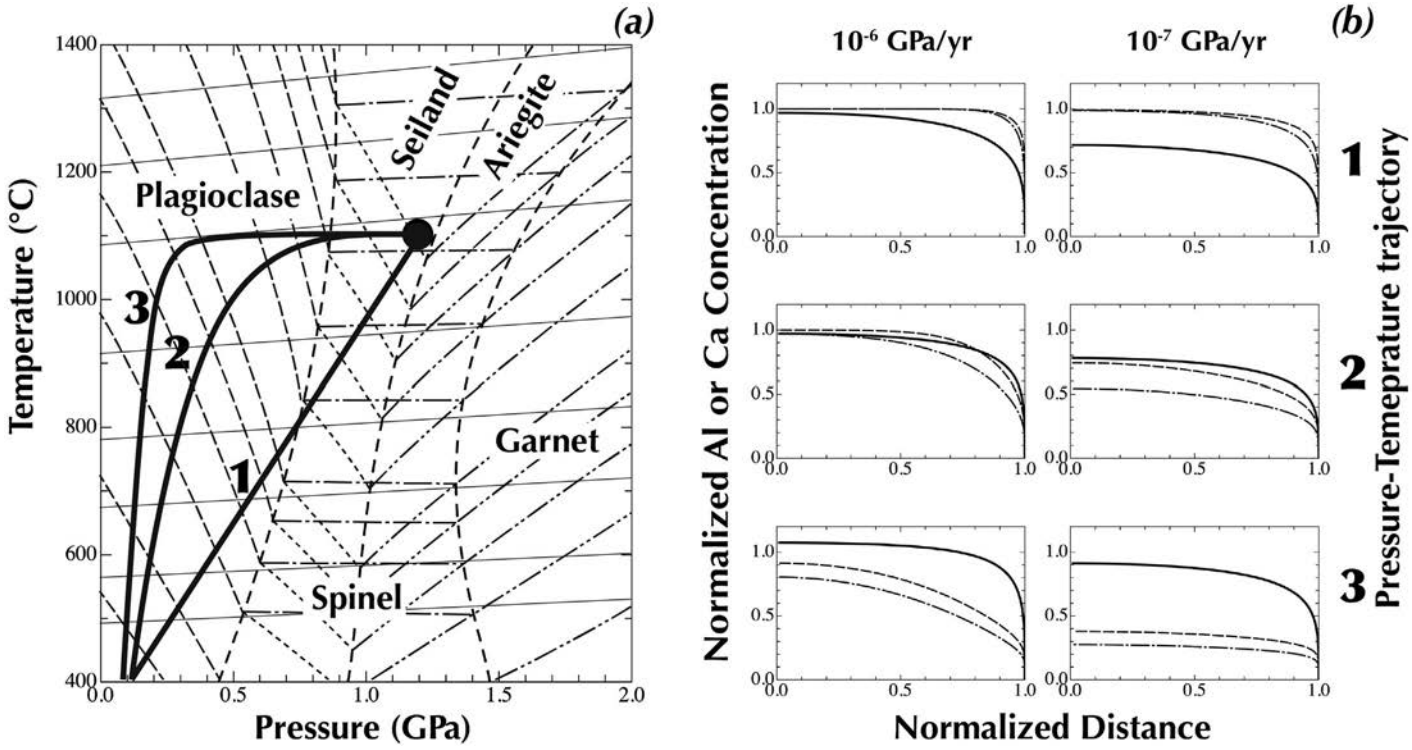

Fig. A2. Modeling of the Al and Ca zoning in a spherical orthopyroxene frozen during decompression and cooling for two decompression rates. (a) Assumed pressure–temperature path, thick lines with number attached, from the initial condition of 1.2 GPa pressure and 1100 °C, indicated with solid circle. (b) Frozen Al profiles shown by a dashed line for the olivine-present system and by a dot–dashed line for the plagioclase-present system, and frozen Ca profiles shown by a thick solid line. Decompression rates are 10^{-4} GPa/year (left panels) and 10^{-5} GPa/year (right panels), and numbers 1 to 3 indicate the decompression and cooling paths shown in (a). The distance from the core (0.0) of orthopyroxene is normalized by its half size, and the rim is 1.0. The concentrations of Al and Ca are normalized by the initial values. In (a), the facies boundaries are shown by thick dashed lines: Garnet = garnet peridotite facies, Spinel = spinel peridotite facies, Plagioclase = plagioclase peridotite facies, Seilandite = Seilandite subfacies, and Ariegite = Ariegite subfacies. The Al isopleths are shown as dashed, dot–dashed, and double-dot–dashed lines for the plagioclase, spinel, and garnet peridotite facies, respectively, and short-dashed and double-dot–dashed lines for the Seiland and Ariegite subfacies, respectively. The Ca isopleths are shown with thin lines. Values for the isopleths are not shown so as not to complicate the diagram.

magnitude slower than in olivine (Coogan et al., 2005). Exsolution of clinopyroxene should be taken into consideration but is ignored. Because of the simple system, the weakly constrained diffusion coefficients of Al and Ca, and the assumption of no exsolution of clinopyroxene, an exact matching between observed and modeled profiles was not attempted, but the possible pressure–temperature (P–T) paths and approximate rates of decompression are constrained. The P–T paths were varied from cooling with limited decompression through linear cooling with decompression to nearly isothermal decompression (Fig. A2a). The rates of decompression were varied from 10^{-4} to 10^{-8} GPa/year (0.3 to 3.0 × 10^{-5} m/year). Frozen profiles for several pairs of P–T paths and decompression rates for an initial condition of 1.2 GPa and 1100 °C and a final condition of 0.1 GPa and 300 °C are shown in Fig. A2b.

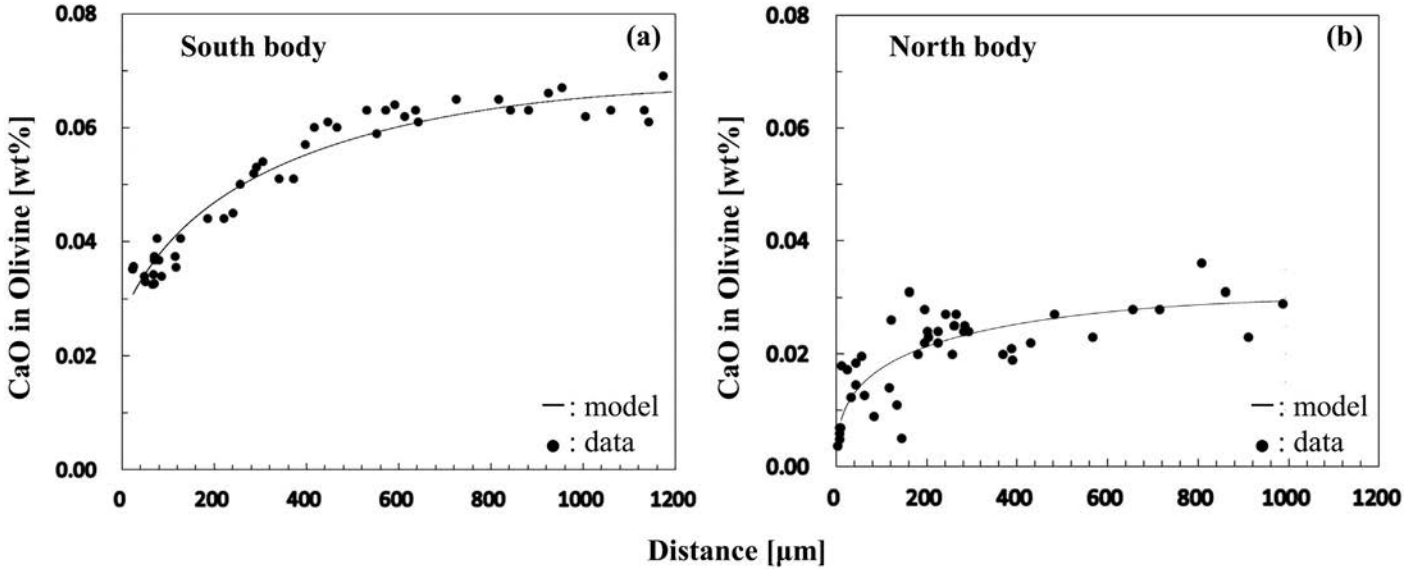

Fig. A3. Modeling of the Ca zoning in olivine in contact with clinopyroxene, frozen during cooling to constrain the cooling rate by reproducing the observed profiles shown in dots. A profile for olivine from the southern body is shown in (a) and one from the northern body in (b).

Examining the full range of decompression rates and the various patterns of decompression path, we found that decompression rates that reasonably reproduce the observed contrasts between the Al and Ca zoning are 10^{-5} GPa/year (0.3 m/year) at 1200 °C for the southern body, and 10^{-6} GPa/year (0.03 m/year) at 1100 °C for the northern body. In both cases, the P–T trajectory must be nearly isothermal at high pressures (>0.3 GPa), followed by rapid cooling at lower pressures (<0.3 GPa).

Appendix C

In this appendix we estimate the rates of cooling by reproducing the Ca zoning in olivine in contact with clinopyroxene (Figs. 10 and A3). The model assumes constant cooling and local equilibrium at the interface with clinopyroxene, constrained by the geothermobarometer recalibrated using the experimental results of Köhler and Brey (1990) (Appendix A). The diffusion coefficient of Ca in olivine is that given by Coogan et al. (2005). We examined the zoning of Ca in olivines from the southern to northern bodies and obtained cooling rates of 5×10^{-4} K/year at 800 °C and 10^{-6} K/year at 650 °C, respectively (Fig. A3).

References

Abramson, E.H., Brown, J.M., Slutsky, L.J., Zaug, J., 1997. The elastic constants of San Carlos olivine to 17 GPa. J. Geophys. Res. Solid Earth 102, 12253–12263.

Artemieva, I.M., 2009. The continental lithosphere: reconciling thermal, seismic, and petrologic data. Lithos 109, 23–46.

Bodinier, J.L., 1988. Geochemistry and petrogenesis of the Lanzo peridotite body, western Alps. Tectonophysics 149, 67–88.

Bodinier, J.L., Menzies, M.A., Thirlwall, M.F., 1991. Continental to oceanic mantle transition—REE and Sr-Nd isotopic geochemistry of the Lanzo lherzolite massif. J. Petrol, Specia. Lherzolites Issue 191–210.

Borghini, G., Fumagalli, P., Rampone, E., 2010. The stability of plagioclase in the upper mantle: subsolidus experiments on fertile and depleted lherzolite. J. Petrol. 51, 229–254.

Borghini, G., Fumagalli, P., Rampone, E., 2011. The geobarometric significance of plagioclase in mantle peridotites: a link between nature and experiments. Lithos 126, 42–53.

Boudier, F., 1972. Relations lherzolites-gabbro-dunite dans le massif de Lanzo (Alpes Piémontaises): exemple de fusion partielle. Thèse 3° cycle, Nantes. p. 118.

Boudier, F., 1976. Le massif lherzolitique de Lanzo (Alpes piémontaises). Etude structurale et pétrologique. Etat, Nantes, Université de Nantes, p. 163 These doct.

Boudier, F., 1978. Structure and petrology of the Lanzo peridotite massif (Piedmont Alps). Geol. Soc. Am. Bull. 89, 1574–1591.

Boudier, F., Nicolas, A., 1972. Fusion partielle gabbroique dans la lherzolite de Lanzo (Alps piédmontaise). Schweiz. Mineral. Petrogr. Mitt. 52, 39–56.

Boudier, F., Nicolas, A., 1977. Structural controls on partial melting in the Lanzo peridotite. In: Dick, J.J.B. (Ed.), Magma Genesis, State Oregon. 96. Department of Geology and Mineral Industries, pp. 63–79.

Brey, G.P., Köhler, T., 1990. Geothermobarometry in four-phase lherzolites II. New thermobarometers, and practical assessment of existing thermobarometers. J. Petrol. 31, 1353–1378.

Chai, M., Brown, J.M., Slutsky, L.J., 1997. The elastic constants of an aluminous orthopyroxene to 12.5 GPa. J. Geophys. Res. Solid Earth 102, 14779–14785.

Chakraborty, S., 2010. Diffusion coefficients in olivine, wadsleyite and ringwoodite. Rev. Mineral. Geochem. 72, 603–639.

Cherniak, D.J., 2010. Cation diffusion in feldspar. Rev. Mineral. Geochem. 72, 691–728.

Cherniak, D.J., Dimanov, A., 2010. Diffusion in pyroxene, mica and amphibole. Rev. Mineral. Geochem. 72, 641–690.

Collins, M.D., Brown, J.M., 1998. Elasticity of an upper mantle clinopyroxene. Phys. Chem. Miner. 26, 7–13.

Coogan, L.A., Hain, A., Stahl, S., Chakraborty, S., 2005. Experimental determination of the diffusion coefficient for calcium in olivine between 900°C and 1500°C. Geochim. Cosmochim. Acta 69, 3683–3694.

Debret, B., Nicollet, C., Andreani, M., Schwartz, S., Godard, M., 2013. Three steps of serpentinization in an eclogitized oceanic serpentinization front (Lanzo Massif–Western Alps). J. Metamorph. Geol. 31, 165–186.

Dodson, M.H., 1973. Closure temperature in cooling geochronological and petrological systems. Contrib. Mineral. Petrol. 40, 259–274.

Faul, U.H., Jackson, I., 2005. The seismological signature of temperature and grain size variations in the upper mantle. Earth Planet. Sci. Lett. 234, 119–134.

Fischer, K.M., Ford, H.A., Abt, D.L., Rychert, C.A., 2010. The lithosphere-asthenosphere boundary. Annu. Rev. Earth Planet. Sci. 38, 551–575.

Fumagalli, P., Borghini, G., Rampone, E., Poli, S., 2017. Experimental calibration of Forsterite–Anorthite–Ca-Tschermak–Enstatite (FACE) geobarometer for mantle peridotites. Contrib. Mineral. Petrol. 172, 38. https://doi.org/10.1007/s00410-017-1352-2.

Ganguly, J., Ito, M., Zhang, X., 2007. Cr diffusion in orthopyroxene: Experimental determination, ^{53}Mn–^{53}Cr thermochronology, and planetary applications. Geochim. Cosmochim. Acta 71, 3915–3925.

Gasparik, T., 1984. Two-pyroxene thermobarometry with new experimental data in the system CaO-MgO-Al_2O_3-SiO_2. Contrib. Mineral. Petrol. 87, 87–97.

Gasparik, T., 1987. Orthopyroxene thermobarometry in simple and complex systems. Contrib. Mineral. Petrol. 96, 357–370.

Gasparik, T., 2000. An internally consistent thermodynamic model for the system CaO-MgO-Al_2O_3-SiO_2 derived primarily from phase equilibrium data. J. Geol. 108, 103–119.

Gasparik, T., 2003. Phase Diagrams for Geoscientists. Springer, Berlin, Heidelberg, New York, p. 462.

Grove, T.L., Baker, M.B., Kinzler, R.J., 1984. Coupled CaAl-NaSi diffusion in plagioclase feldspar: experiments and application to cooling rate speedometry. Geochim. Cosmochim. Acta 48, 2113–2121.

Guarnieri, L., Nakamura, E., Piccardo, G.B., Sakaguchi, C., Shimizu, N., Vannucci, R., Zanetti, A., 2012. Petrology, trace element and SR, Nd, Hf isotope geochemistry of the North Lanzo peridotite massif (Western Alps, Italy). J. Petrol. 53, 2259–2306.

Higgie, K., Tommasi, A., 2014. Deformation in a partially molten mantle: constraints from plagioclase lherzolites from Lanzo, western Alps. Tectonophysics 615-616, 167–181.

Hirschmann, M., 1991. Thermodynamics of multicomponent olivines and the solution properties of (Ni,Mg,Fe)$_2SiO_4$ and (Ca,Mg,Fe)$_2SiO_4$ olivine. Am. Mineral. 68, 1232–1248.

Hirschmann, M.M., 2000. Mantle solidus: Experimental constraints and the effects of peridotite composition. Geochem. Geophys. Geosyst. 1 2000GC000070.

Hirschmann, M.M., 2010. Partial melt in the oceanic low velocity zone. Phys. Earth Planet. Inter. 179, 60–71.

Hirth, G., Kohlstedt, D.L., 1996. Water in the oceanic upper mantle: implications for rheology, melt extraction and the evolution of the lithosphere. Earth Planet. Sci. Lett. 144, 93–108.

Jollands, M.C., Müntener, O., 2019. Testing orthopyroxene diffusion chronometry on rocks from the Lanzo Massif (Italian Alps). J. Geophys. Res. Solid Earth 124, 7822–7841.

Kaczmarek, M.A., Müntener, O., 2008. Juxtaposition of melt impregnation and high-temperature shear zones in the upper mantle; field and petrological constraints from the Lanzo Peridotite (Northern Italy). J. Petrol. 49, 2187–2220.

Kaczmarek, M.A., Müntener, O., 2010. The variability of peridotite composition across a mantle shear zone (Lanzo massif, Italy): interplay of melt focusing and deformation. Contrib. Mineral. Petrol. 160, 663–679.

Kaczmarek, M.A., Tommasi, A., 2011. Anatomy of an extensional shear zone in the mantle, Lanzo massif, Italy. Geochem. Geophys. Geosyst. 12. https://doi.org/10.1029/2011GC003627.

Kaczmarek, M.A., Müntener, O., Rubatto, D., 2008. Trace element chemistry and U–Pb dating of zircons from oceanic gabbros and their relationship with whole rock composition (Lanzo, Italian Alps). Contrib. Mineral. Petrol. 155, 295–312.

Karato, S., 2012. On the origin of asthenosphere. Earth Planet. Sci. Lett. 321-322, 95–103.

Karato, S.I., Jung, H., 1998. Water, partial melting and the origin of the seismic low velocity and high attenuation zone in the upper mantle. Earth Planet. Sci. Lett. 157, 193–207.

Katz, R.F., Spiegelman, M., Langmuir, C.H., 2003. A new parameterization of hydrous mantle melting. Geochem. Geophys. Geosyst. 4. https://doi.org/10.1029/2002GC000433.

Kawakatsu, H., Utada, H., 2017. Seismic and electrical signatures of the lithosphere–asthenosphere system of the normal oceanic mantle. Annu. Rev. Earth Planet. Sci. 45, 139–167.

Kawakatsu, H., Kumar, P., Takei, Y., Shinohara, M., Kanazawa, T., Araki, E., Suyehiro, K., 2009. Seismic evidence for sharp lithosphere-asthenosphere boundaries of oceanic plates. Science 324, 499–502.

Kienast, J.R., Pognante, U., 1988. Chloritoid-bearing assemblages in eclogitised metagabbros of the Lanzo peridotite body (western Italian Alps). Lithos 21, 1–11.

Klemme, S., O'Neill, H.S., 2000. The effect of Cr on the solubility of Al in orthopyroxene: experiments and thermodynamic modeling. Contrib. Mineral. Petrol. 140, 84–98.

Köhler, T.P., Brey, G., 1990. Calcium exchange between olivine and clinopyroxene calibrated as a geothermobarometer for natural peridotites from 2 to 60 kb with applications. Geochim. Cosmochim. Acta 54, 2375–2388.

Lagabrielle, Y., Fudal, S., Kienast, J.R., 1989. La couverture océanique de ultrabasites de Lanzo (Alpes occidentales): arguments lithostratigraphiques. Geodinamica Acta (Paris) 3, 43–55.

Lambert, I.B., Wyllie, P.J., 1970. Low-velocity zone of the Earth's mantle: incipient melting caused by water. Science 169, 764–766.

Lindsley, D.H., 1983. Pyroxene thermometry. Am. Mineral. 68, 477–493.

Llovet, X., Fernández-Varea, J.M., Sempau, J., Salvat, F., 2005. Monte Carlo simulation of X-ray emission using the general-purpose code PENELOPE. Surface and Interface Analysis: An International Journal devoted to the development and application of techniques for the analysis of surfaces, interfaces and thin films. 37 pp. 1054–1058.

Lorand, J.P., Keays, R.R., Bodinier, J.L., 1993. Copper and noble metal enrichment across the lithosphere-asthenosphere boundary of mantle diapirs: evidence from the Lanzo lherzolite massif. J. Petrol. 34, 1111–1140.

McKenzie, D., Jackson, J., Priestley, K., 2005. Thermal structure of oceanic and continental lithosphere. Earth Planet. Sci. Lett. 233, 337–349.

Mierdel, K., Keppler, H., Smyth, J.R., Langenhorst, F., 2007. Water solubility in aluminous orthopyroxene and the origin of Earth's asthenosphere. Science 315, 364–368.

Müntener, O., Piccardo, G.B., 2003. Melt migration in ophiolitic peridotites: the message from Alpine-Apennine peridotites and implications for embryonic ocean basins. Geol. Soc. Lond. Spec. Publ. 218, 69–89.

Müntener, O., Piccardo B., G., Polino, R., Zanetti, A., 2005. Revisiting the Lanzo peridotite (NW-Italy): 'athenospherization' of ancient mantle lithosphere. Ofioliti 30, 111–124.

Nagata, J., Goto, A., Obata, M., 1983. The parabolic pattern of chromium partitioning observed between pyroxenes and spinel from ultramafic rocks and its petrologic significance. Contrib. Mineral. Petrol. 82, 42–51.
Nicolas, A., 1984. Lherzolites of the Western Alps: a structural review. In: Kornprobst, J. (Ed.), 5th International Kimberlite Conference Proceedings. Elsevier, Amsterdam, pp. 333–345.
Nicolas, A., Bouchez, J.L., Boudier, F., 1972. Interprétation cinématique des deformations plastiques dans le massif de lherzolite de Lanzo (Alpes Piémontaises): comparaison ave d'autres massifs. Tectonophysics 14, 143–171.
Nimis, P., Grütter, H., 2010. Internally consistent geothermometers for garnet peridotites and pyroxenites. Contrib. Mineral. Petrol. 159, 411–427.
Niu, Y., Green, D.H., 2018. The petrological control on the lithosphere-asthenosphere boundary (LAB) beneath ocean basins. Earth Sci. Rev. 185, 301–307.
Obata, M., 1976. The solubility of Al_2O_3 in orthopyroxenes in spinel and plagioclase peridotites and spinel pyroxenite. Am. Mineral. 61, 804–816.
Ozawa, K., 1989. Stress-induced Al–Cr zoning of spinel in deformed peridotites. Nature 338, 141–144.
Ozawa, K., 1997. P-T history of an ascending mantle peridotite constrained by Al zoning in orthopyroxene: a case study in the Horoman peridotite complex, Hokkaido, northern Japan. Mem. Geol. Soc. Japan 47, 107–122.
Ozawa, K., 2004. Thermal history of the Horoman peridotite complex: a record of thermal perturbation in the lithospheric mantle. J. Petrol. 45, 253–273.
Ozawa, K., Takahashi, N., 1995. PT history of a mantle diapir: the Horoman peridotite complex, Hokkaido, northern Japan. Contrib. Mineral. Petrol. 120, 223–248.
Pelletier, L., Müntener, O., 2006. High-pressure metamorphism of the Lanzo peridotite and its oceanic cover, and some consequences for the Sesia–Lanzo zone (northwestern Italian Alps). Lithos 90, 111–130.
Piccardo, G.B., Zanetti, A., Müntener, O., 2007. Melt/peridotite interaction in the Southern Lanzo peridotite: field, textural and geochemical evidence. Lithos 94, 181–209.
Piccardo, G.B., Vannucci, R., Guarnieri, L., 2009. Evolution of the lithospheric mantle in an extensional setting: Insights from ophiolitic peridotites. Lithosphere 1, 81–87.
Pognante, U., Rösli, U., Toscani, L., 1985. Petrology of ultramafic and mafic rocks from the Lanzo peridotite body (Western Alps). Lithos 18, 201–214.
Press, F., 1959. Some implications on mantle and crustal structure from G waves and love waves. J. Geophys. Res. 64, 565–568.
Ringwood, A.E., 1962. A model for the upper mantle. J. Geophys. Res. 67, 857–867.
Rubatto, D., Müntener, O., Barnhoorn, A., Gregory, C., 2008. Dissolution-reprecipitation of zircon at low-temperature, high-pressure conditions (Lanzo Massif, Italy). Am. Mineral. 93, 1519–1529.
Rychert, C.A., Shearer, P.M., 2009. A global view of the lithosphere-asthenosphere boundary. Science 324, 495–498.
Sack, R.O., Ghiorso, M.S., 1994. Thermodynamics of multicomponent pyroxenes: II. Phase relations in the quadrilateral. Contrib. Mineral. Petrol. 116, 287–300.
Sanfilippo, A., Tribuzio, R., Tiepolo, M., 2014. Mantle–crust interactions in the oceanic lithosphere: Constraints from minor and trace elements in olivine. Geochim. Cosmochim. Acta 141, 423–439.
Sanfilippo, A., Tribuzio, R., Ottolini, L., Hamada, M., 2017. Water, lithium and trace element compositions of olivine from Lanzo south replacive mantle dunites (Western Alps): New constraints into melt migration processes at cold thermal regimes. Geochim. Cosmochim. Acta 214, 51–72.
Sanfilippo, A., Salters, V., Tribuzio, R., Zanetti, A., 2019. Role of ancient, ultra-depleted mantle in Mid-Ocean-Ridge magmatism. Earth Planet. Sci. Lett. 511, 89–98.
Sato, Y., Ozawa, K., 2019. Reconstruction of the lithosphere-asthenosphere boundary zone beneath Ichinomegata maar, Northeast Japan, by geobarometry of spinel peridotite xenoliths. Am. Mineralogist: J. Earth Planet. Mater. 104, 1285–1306.
Smith, D., Barron, B.R., 1991. Pyroxene-garnet equilibration during cooling in the mantle. Am. Mineral. 76, 1950–1963.
Spetzler, H., Anderson, D.L., 1968. The effect of temperature and partial melting on velocity and attenuation in a simple binary system. J. Geophys. Res. 73, 6051–6060.
Suhr, G., Kelemen, P., Paulick, H., 2008. Microstructures in Hole 1274A peridotites, ODP Leg 209, Mid-Atlantic Ridge: Tracking the fate of melts percolating in peridotite as the lithosphere is intercepted. Geochem. Geophys. Geosyst. 9. https://doi.org/10.1029/2007GC001726.
Takahashi, E., Shimazaki, T., Tsuzaki, Y., Yoshida, H., 1993. Melting study of a peridotite KLB-1 to 6.5 GPa and the origin of basaltic magmas. Phil. Trans. R. Soc. London A342, 105–120.
Takazawa, E., Frey, F., Shimizu, N., Obata, M., 1996. Evolution of the Horoman peridotite (Hokkaido, Japan): implications from pyroxene compositions. Chem. Geol. 134, 3–26.
Takei, Y., 2019. Phase-field modeling of grain boundary premelting. J. Geophys. Res. Solid Earth 124, 8057–8076.
Taylor, W.R., 1998. An experimental test of some geothermometer and geobarometer formulations for upper mantle peridotites with application to the thermobarometry of fertile lherzolite and garnet websterite. Neues Jahrbuch für Mineralogie-Abhandlungen 172, 381–408.
Wells, P.R., 1977. Pyroxene thermometry in simple and complex systems. Contrib. Mineral. Petrol. 62, 129–139.